Consecutive Ruptures on a Complex Conjugate Fault System During the 2018 Gulf of Alaska Earthquake

Shinji Yamashita[1,1,1,1], Yuji Yagi[1,1,1,1], Ryo Okuwaki[1,1,1,1], Kousuke Shimizu[1,1,1,1], Ryoichiro Agata[2,2,2,2], and Yukitoshi Fukahata[3,3,3,3]

[1]University of Tsukuba
[2]Japan Agency for Marine-Earth Science and Technology
[3]Kyoto University

November 30, 2022

Abstract

We developed a flexible finite-fault inversion method for teleseismic P waveforms to obtain a detailed rupture process of a complex multiple-fault earthquake. We estimate the distribution of potency-rate density tensors on an assumed model fault plane to clarify rupture evolution processes, including variations of fault geometry. We applied our method to the 23 January 2018 Gulf of Alaska earthquake, setting the model fault area to fit the distribution of aftershocks occurring within one week of the mainshock. The obtained source model, which successfully explained the complex teleseismic P waveforms, shows that the 2018 earthquake ruptured a conjugate system of N-S and E-W faults. The spatiotemporal rupture evolution indicates irregular rupture behavior involving a multiple-shock sequence, which is likely associated with discontinuities in the fault geometry that originated from E-W sea-floor fracture zones and N-S plate-bending faults.

Consecutive Ruptures on a Complex Conjugate Fault System During the 2018 Gulf of Alaska Earthquake

Shinji Yamashita[1, *], Yuji Yagi[2, **], Ryo Okuwaki[2, 3, 4], Kousuke Shimizu[1], Ryoichiro Agata[5], and Yukitoshi Fukahata[6]

[1]Graduate School of Life and Environmental Sciences, University of Tsukuba, Tsukuba, Ibaraki 305-8572, Japan

[2]Faculty of Life and Environmental Sciences, University of Tsukuba, Tsukuba, Ibaraki 305-8572, Japan

[3]Mountain Science Center, University of Tsukuba, Ibaraki 305-8572, Japan

[4]COMET, School of Earth and Environment, University of Leeds, Leeds LS2 9JT, UK

[5]Japan Agency for Marine-Earth Science and Technology, 3173-25 Showa-machi, Kanazawa-ku, Yokohama 236-0001, Japan

[6]Disaster Prevention Research Institute, Kyoto University, Uji, Kyoto 611-0011, Japan

[*]Corresponding author: Shinji Yamashita (syamashita@geol.tsukuba.ac.jp)

[**]Second corresponding author: Yuji Yagi (yagi-y@geol.tsukuba.ac.jp)

ABSTRACT

We developed a flexible finite-fault inversion method for teleseismic *P* waveforms to obtain a detailed rupture process of a complex multiple-fault earthquake. We estimate the distribution of potency-rate density tensors on an assumed model plane to clarify rupture evolution processes, including variations of fault geometry. We applied our method to the 23 January 2018 Gulf of Alaska earthquake by representing slip on a projected horizontal model plane at a depth of 33.6 km to fit the distribution of aftershocks occurring within one week of the mainshock. The obtained source model, which successfully explained the complex teleseismic *P* waveforms, shows that the 2018 earthquake ruptured a conjugate system of N-S and E-W faults. The spatiotemporal rupture evolution indicates irregular rupture behavior involving a multiple-shock sequence, which is likely associated with discontinuities in the fault geometry that originated from E-W sea-floor fracture zones and N-S plate-bending faults.

Introduction

The 23 January 2018 Gulf of Alaska earthquake (moment-magnitude M_W 7.9 [1]) struck offshore Kodiak Island (55.9097°N, 149.0521°W, 10.4 km depth; Alaska Earthquake Center, AEC [1]), in the seaward-region of the Alaska-Aleutian subduction zone. The Global Centroid Moment Tensor (GCMT) project [2,3] reported that the 2018 Gulf of Alaska earthquake had strike-slip faulting with a large non-double-couple component (47%). Aftershock seismicity determined by the AEC [1] shows a lineation extending about 120 km N-S near the epicenter and two aftershock clusters centered about 60 km northeast and about 50 km west from the epicenter (Fig. 1). The GCMT

solutions of aftershocks are dominated by strike-slip faulting, but include normal and reverse faulting (Fig. 1).

Several pioneering studies that built finite-fault models based on the aftershock distribution demonstrated that the 2018 Gulf of Alaska earthquake ruptured a quasi-orthogonal multiple-fault system oriented approximately N-S and E-W [4–8]. However, it is difficult to adopt a reasonable fault model because the fault model parametrization, number of fault segments, and fault geometries differ by study, partly due to the spatial spread of the aftershock distribution (Fig. 1). Based on the static slip distribution estimated from Global Navigation Satellite System and tsunami data, major slips occurred on E-W-striking segments [5,7,8]. Finite-fault inversions estimated that the maximum slip occurred around the boundary between the crust and uppermost mantle in the N-S-oriented segment [4,6], which would have played a significant role in tsunami generation. However, it remains challenging to adequately explain the complex characteristics of the observed teleseismic body waveforms by conventional finite-fault inversion methods due to the uncertainty on the fault geometry, which lead to significant model errors.

In the framework of finite-fault waveform inversion, uncertainties on the Green's function and fault geometry have been the major sources of model errors [9–13]. Those due to uncertainty on the Green's function arose from a discrepancy between the true and calculated Green's functions. To mitigate the effect of this uncertainty, Yagi and Fukahata [13] explicitly introduced the error term of the Green's function into the data covariance matrix. As a result, their inversion framework allowed the stable estimation of the spatiotemporal distribution of slip-rate, usually without the non-negative slip-rate constraint, which had been commonly applied in conventional waveform inversion methods to obtain a plausible solution [14,15].

Model errors due to uncertainty on the fault geometry arose from inappropriate assumptions about the fault geometry [11,12]. For strike-slip earthquakes, many seismic stations are distributed in the vicinity of nodal planes where the radiation pattern is sensitive to the assumed fault geometry. An obtained solution can easily be distorted by inappropriate assumptions of strike and dip [12]. These effects can be mitigated by increasing the degrees of freedom in the assumed seismic source model. Shimizu et al. [12] proposed an inversion method to express slip vectors on the assumed model plane as the seismic potency tensor. Because their method adopts a linear combination of five basis double-couple components [16], the slip direction is not restricted to the two slip components compatible with the fault direction. Of course, the true fault geometry should be compatible with the actual slip direction. Whilst the teleseismic *P*-wave Green's function is insensitive to slight changes in the absolute source location, it is sensitive to the assumed focal mechanisms [12,16,17], and their inversion method enabled the spatiotemporal resolution of not only the detailed rupture evolution, but also variation of the focal mechanism, including information on the fault geometry, which may differ from the assumed model plane.

In this study, we developed a flexible finite-fault inversion framework that can estimate both the rupture evolution and focal mechanism of earthquakes that ruptured along multiple complex fault segments. This method incorporates appropriate smoothness constraints and a high-degree-of-freedom planar model into the inversion framework of Shimizu et al. [12]. Application of our framework to the 2018 Gulf of Alaska earthquake shows that our source model sufficiently reproduced the observed complex waveforms without assumptions on fault geometry. The model also clarified multiple, distinct rupture events in the conjugate fault system that have not been revealed by conventional finite-fault inversion methods.

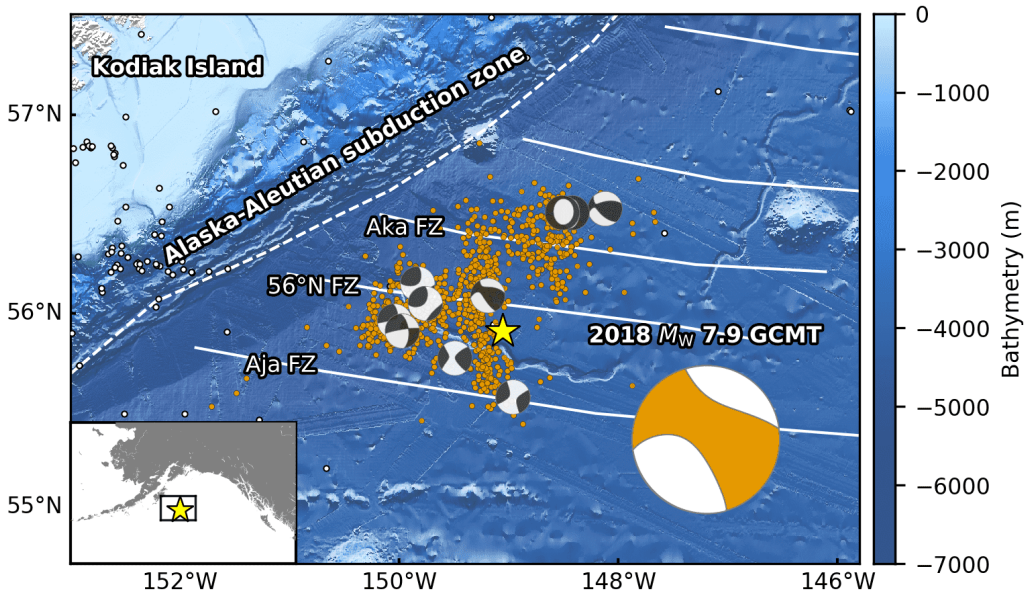

Figure 1. Overview of the source region of the 2018 Gulf of Alaska earthquake. The star is the mainshock epicenter, orange dots are aftershocks ($M \geq 3$) that occurred within one week of the mainshock, and white dots show background seismicity before the mainshock ($M \geq 3.5$, 1 January 2008 to 22 January 2018); all epicentral locations are from AEC [1]. The 'beachball' diagrams show the GCMT solutions for the mainshock (large, bottom right) and aftershocks with $M \geq 3.5$. White dashed lines represent plate boundaries [18], and white solid lines represent fracture zones [19,20]. The background bathymetry is derived from the GEBCO 2020 Grid [21]. The inset map shows the regional setting. This figure was made with matplotlib (v3.1.1) [48], ObsPy (v1.1.0) [49], and Generic Mapping Tools (v5.4.5) [50].

Method

In the inversion framework of Shimizu et al. [12], the seismic waveform u_j observed at a station j is given by

$$u_j(t) = \sum_{q=1}^{5} \int_S \left(G_{qj}(t,\boldsymbol{\xi}) + \delta G_{qj}(t,\boldsymbol{\xi})\right) * \dot{D}_q(t,\boldsymbol{\xi})\, d\boldsymbol{\xi} + e_{bj}(t), \qquad (1)$$

where G_{qj} is the calculated Green's function of the qth basis double-couple component, δG_{qj} is the model error on G_{qj} [13], $\dot{D}_q$ is the qth potency-rate density function on the assumed model plane S, e_{bj} is background and instrumental noise, $\boldsymbol{\xi}$ represents a position on S, and $*$ denotes the convolution operator in the time domain.

Shimizu et al. [12] represented the assumed model plane S as a rectangle horizontally covering the seismic source region. However, for earthquakes with complex fault geometries, such as the 2018 Gulf of Alaska earthquake, such a horizontal rectangular model plane includes areas beyond the seismic source region. Therefore, we further extended their inversion framework such that a horizontal non-rectangular model plane can be set according to the shape of the ruptured region as estimated from other information (e.g., aftershock seismicity). In other words, we introduced *a priori* information about the possible ruptured area into the inversion framework. In

numerical tests, the use of a non-rectangular model plane improved spatial resolution and computation costs compared to a rectangular one (see Supplementary Material S1 and Figs. S1–S4).

In general, inversions are stabilized by adding smoothness constraints either implicitly or explicitly [22–24]. In the formulation of Shimizu et al. [12], the smoothness constraints on each potency-rate density function $\dot{D}_q$ in space and time are represented as

$$\nabla^2 \dot{D}_q(t,\xi) + \alpha_q = 0, \qquad (2)$$

$$\frac{\partial^2}{\partial t^2} \dot{D}_q(t,\xi) + \beta_q = 0, \qquad (3)$$

where α_q and β_q are assumed to be Gaussian noise with zero mean and covariances of $\sigma^2\mathbf{I}$ and $\tau^2\mathbf{I}$, respectively, where $\mathbf{I}$ is an $M \times M$ (M is the number of model parameters) unit matrix. Because they introduced identical Gaussian distributions for all basis components and determined the optimal values of the hyperparameters σ^2 and τ^2 by Akaike's Bayesian information criterion [23,25], the potency-rate density functions of basis components with relatively high amplitudes become smoother than those of basis components with relatively low amplitudes, which may bias the solution. Thus, when the amplitudes of the potency-rate density functions differ for each basis component, the standard deviations of the smoothness constraints should depend on the amplitude of each basis component.

In this study, we set the standard deviation of the smoothness constraints for each basis double-couple component to be proportional to its amplitude. That is, instead of α_q and β_q, we directly introduced Gaussian noise with zero mean and covariances $\sigma_q^2\mathbf{I}$ and $\tau_q^2\mathbf{I}$, respectively, as

$$\sigma_q^2\mathbf{I} = k^2 m_q^2 \sigma^2 \mathbf{I}, \qquad (4)$$

$$\tau_q^2\mathbf{I} = k^2 m_q^2 \tau^2 \mathbf{I}, \qquad (5)$$

where k is a scaling factor and m_q is the total potency of the qth basis double-couple component, which is independently derived from the moment tensor solution. To avoid extremely small standard deviations destabilizing the solution, we adjusted $k|m_q|$ so that it does not fall below 10% of its maximum absolute value. Following Yagi and Fukahata [13], we determined the hyperparameters σ^2 and τ^2 by Akaike's Bayesian information criterion [23,25]. In numerical tests, these improved smoothness constraints mitigated the excessive smoothing of the dominant basis component imposed by conventional smoothness constraints and, when combined with a non-rectangular model plane, outperformed the conventional framework (see Supplementary Material S1, Figs. S1–S4 and Table S1).

Data and Fault Parameterization

We used teleseismic *P* waveforms (vertical components) recorded at stations with epicentral distances of 30–90° (downloaded from the Incorporated Research Institutions for Seismology Data Management Center). Of these, we selected 78 stations, ensuring a high signal-to-noise ratio and an azimuthal coverage [26] (Fig. 2c), and converted the *P* waveforms to velocity waveforms at a sampling rate of 0.8 s. The theoretical Green's functions for teleseismic body waves were calculated by the method of Kikuchi and Kanamori [16] at a sampling rate of 0.1 s, and the attenuation time constraint t^* for the *P* wave was taken to be 1.0 s. We adopted a 1-D velocity structure derived

from the CRUST1.0 model [27] (see Supplementary Table S2) to calculate the theoretical Green's functions. Following Shimizu et al. [12], we did not low-pass filter the observed waveforms or calculated Green's functions. For the smoothness constraints, we calculated m_q based on the GCMT solution of the 2018 Gulf of Alaska earthquake. The GCMT solution shows that the M1 (strike-slip) component [16] is more prominent than the others (see Supplementary Table S3), including the M4 (dip-slip) component [16] (see Supplementary Fig. S4). The scaling factor k in eqs. (4) and (5) was set such that $min(k|m_q|) = 1$ (Table S3).

Based on the aftershock distribution, the 2018 Gulf of Alaska earthquake is considered to have occurred on a quasi-orthogonal multiple-fault system [4–8]. To cover the high point density area of aftershocks within one week of the event [1] (Fig. 2a), we set up a non-rectangular horizontal model plane with a maximum width and length of 130 km, which was expanded using a bilinear B-spline with a knot spacing of 10 km. We adopted the epicenter as that determined by the AEC [1]: 55.9097°N, 149.0521°W. The depth of the model fault plane was set at 33.6 km according to the GCMT centroid depth. For the inversion analysis, we adopted a potency-rate density function on each knot, each representing a linear combination of B-splines at an interval of 0.8 s. The maximum rupture-front velocity, which defines the rupture starting time at each knot, was set to 7.0 km/s to account for the possibility of supershear rupture propagation. The rupture ending time at each knot was set to 65 s from the origin time based on previous inversion results [4,6]. We evaluated the sensitivity of our model by perturbing the model parameters, and the robustness of the new method (see Supplementary Material S2, and Figs. S5, S6 and S9).

Results

We estimated the spatiotemporal distribution of the potency density tensor for the 2018 Gulf of Alaska earthquake by applying our flexible finite-fault inversion method to teleseismic *P* waveforms. The estimated total moment tensor, calculated by taking the spatial and temporal integrals of the potency-rate density functions, expresses strike-slip faulting, including 36% non-double-couple components (Fig. 2a). The spatial distribution of the potency density tensor, obtained by temporally integrating the potency-rate density functions at each knot, is also dominated by strike-slip focal mechanisms, with a maximum slip of 6 m about 50 km north of the epicenter (Fig. 2a). The moment rate function is elevated over two time periods, separated at 27 s from the origin time: the first period is characterized by three large spikes and the second by numerous smaller spikes (Fig. 2b). The total seismic moment is 14.9×10^{20} N m (M_W 8.05). The synthetic waveforms from the obtained source model well reproduce the observed waveforms (see Supplementary Fig. S11), including those at stations near the nodal planes (Fig. 2d).

Based on the moment rate function and snapshots of the potency-rate density tensors (Figs. 2b and S12, respectively), we report the detailed rupture history by dividing it into main (A, 0–27 s) and secondary rupture stages (B, 27–65 s). Based on the location, timing, and continuity of the rupture, we further identified three phases (A1–A3) during the main stage and five (B1–B5) during the secondary stage (Figs. 3 and 4).

Main Rupture Stage (A)

The initial phase, A1 (0–9 s), started at the hypocenter and propagated bilaterally northward and southward with strike-slip focal mechanisms (snapshot at 2 s in Fig. 3a). Although it is generally difficult to identify the preferred fault plane from the two possible nodal planes in this earthquake, the direction of rupture propagation during phase A1 coincided with the N-S directed nodal plane.

The spatial distribution of focal mechanisms shows that the strike of the fault plane gradually rotated counterclockwise from north to south of the epicenter; we obtained a strike/dip of 174°/82° around 20 km north of the epicenter, but 163°/76° around 20 km south of the epicenter (6 s in Fig. 3a). The northward rupture seems to have stagnated near the 56°N fracture zone [28] (FZ) after about 9 s (Fig. 4a).

Phase A2 (7–27 s) started about 50 km northeast of the epicenter at around 7 s after the origin time and propagated west along the Aka FZ [28] (8 s in Fig. 3a). This rupture direction is consistent with the obtained E-W strike directions (e.g., 10 s in Fig. 3a). The westward rupture propagated to 149.2°W, where the Aka FZ intersects the N-S aftershock lineation, until 11 s, then turned southward, indicating that the N-S strike direction is the preferred fault plane (12 s in Fig. 3a). The southward rupture halted at around 12 s at the same location where the northward rupture of phase A1 had stagnated at about 9 s (Fig. 4a). After 12 s, a discontinuous rupture occurred along the Aka FZ: ruptures propagating southward and northward from the Aka FZ near 148.6°W are detected at around 16 and 20 s, respectively (Fig. 3a). The rupture on the Aka FZ near 149.2°W is again apparent at around 24 s, and gradually ceased by 27 s.

Phase A3 (16–27 s), started about 40 km northwest of the epicenter, near the 56°N FZ, around 16 s after the origin time (Fig. 3a). This rupture propagated bilaterally to the northeast and southwest until around 18 s, then gradually abated until around 20 s. At that time, another western rupture occurred at the northwest end of the model region and propagated to the south (20 s in Fig. 3a), stagnating at the 56°N FZ about 50 km west of the epicenter at around 22 s (24 s in Fig. 3a).

Secondary Rupture Stage (B)

We identified seven peaks in the moment rate function during the secondary rupture stage (Fig. 2b), which we attribute to five phases in the snapshots (Fig. 3b). Phase B1 (28–44 s) occurred along the Aka FZ. In particular, phase B1 ruptures at around 32.8 and 40.0 s were relatively large, and appear as individual peaks in the moment rate function (Figs. 2b and 3b). Phase B2 (44–52 s) mainly ruptured the region west of the epicenter. The rupture at around 44.8 s occurred along the 56°N FZ and that at around 49.6 s struck about 30 km south of the 56°N FZ (Fig. 3b). Phase B3 (53–60 s) occurred mainly northeast of the epicenter, but also struck the intersection of the Aka FZ and the N-S aftershock lineation at around 52.8 s (Fig. 3b). A northward rupture from the Aka FZ was also detected at around 57.6 s. The last peak of the moment rate function corresponds to two independent phases that occurred at around 63.2 s: B4 (62–65 s) ruptured about 20 km south of the Aka FZ and B5 (62–64 s) ruptured about 30 km south of the epicenter (Fig. 3b).

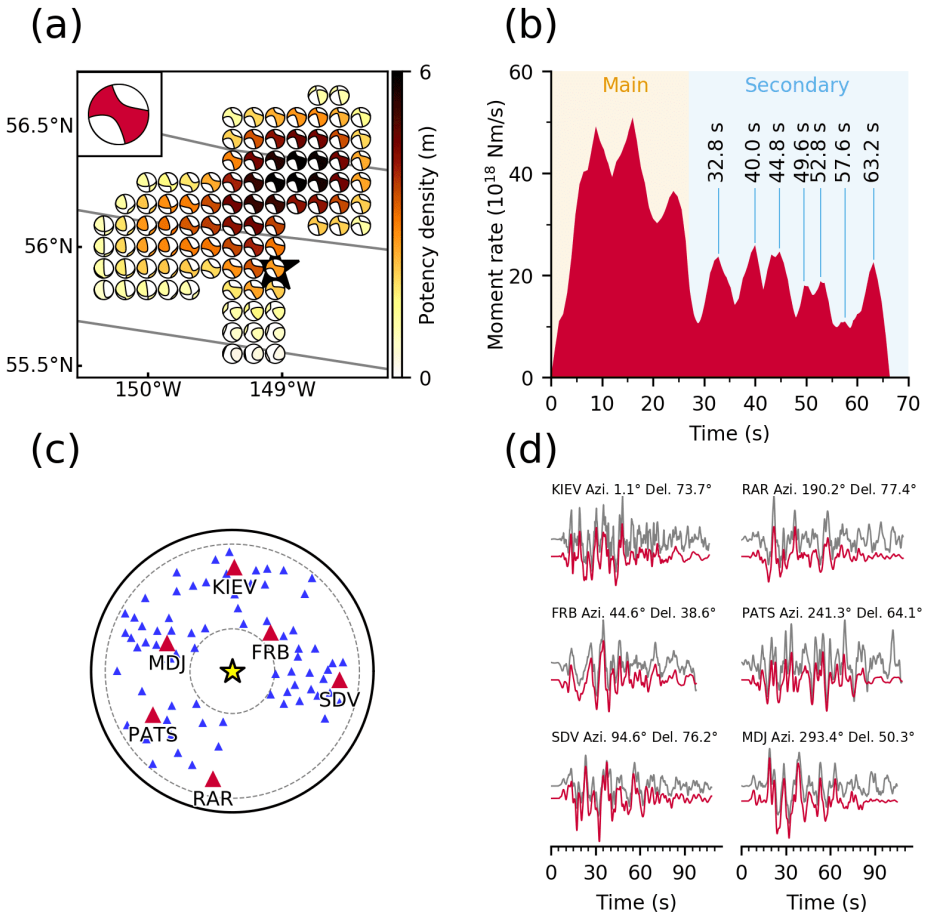

Figure 2. Model setting and summary of results. (a) Map projection of the potency density tensor distribution on the assumed model plane. The star and solid lines indicate the epicenter [1] and fracture zones [19,20], respectively. Inset is the total moment tensor. (b) The moment rate function is divided into the main and secondary rupture stages at 27 s. The individual peaks during the secondary stage correspond to snapshots in Fig. 3b. (c) Azimuthal equidistant projection of the station distribution used in the inversion. The star denotes the epicenter, and triangles denote station locations (waveforms for red stations are shown in (d)). The inner and outer dotted lines show epicentral distances of 30° and 90°, respectively. (d) Comparison of observed waveforms (gray) with synthetic waveforms (red) at the selected stations in (c). Each panel is labeled with the station name, azimuth (Azi.), and epicentral distance (Del.) from the mainshock. Waveform comparisons for all stations are shown in Supplementary Fig. S11. This figure was made with matplotlib (v3.1.1) [48] and ObsPy (v1.1.0) [49].

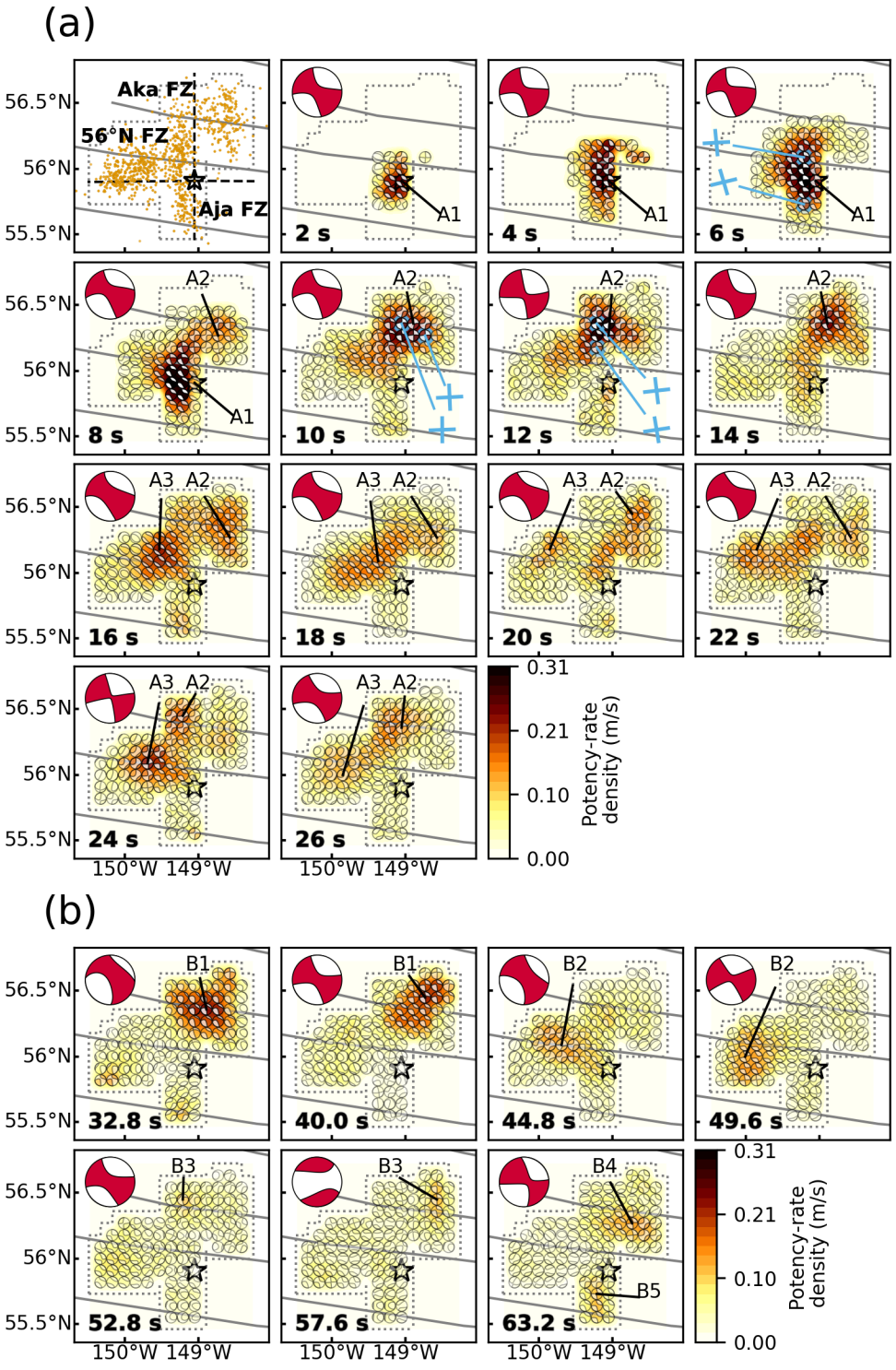

Figure 3. Snapshots of the potency-rate density tensors for (a) the main rupture stage A and (b) the secondary rupture stage B. The corresponding time after onset for each snapshot is noted at the bottom-left of each panel. The dotted line shows the border of the assumed model plane. The star and solid lines indicate the epicenter [1] and fracture zones [19,20], respectively. Blue crosses show the strike directions of small beachball diagrams derived from the potency-rate density tensor. The

top-left panel in (a) is the epicentral distribution of aftershocks ($M \geq 3$) that occurred within one week of the mainshock [1]. The large beachball in each panel indicates the corresponding total moment tensor at each time. The dashed lines on the left-top panel of Fig. 3a are the projection lines used for Fig. 4. This figure was made with matplotlib (v3.1.1) [48] and ObsPy (v1.1.0) [49].

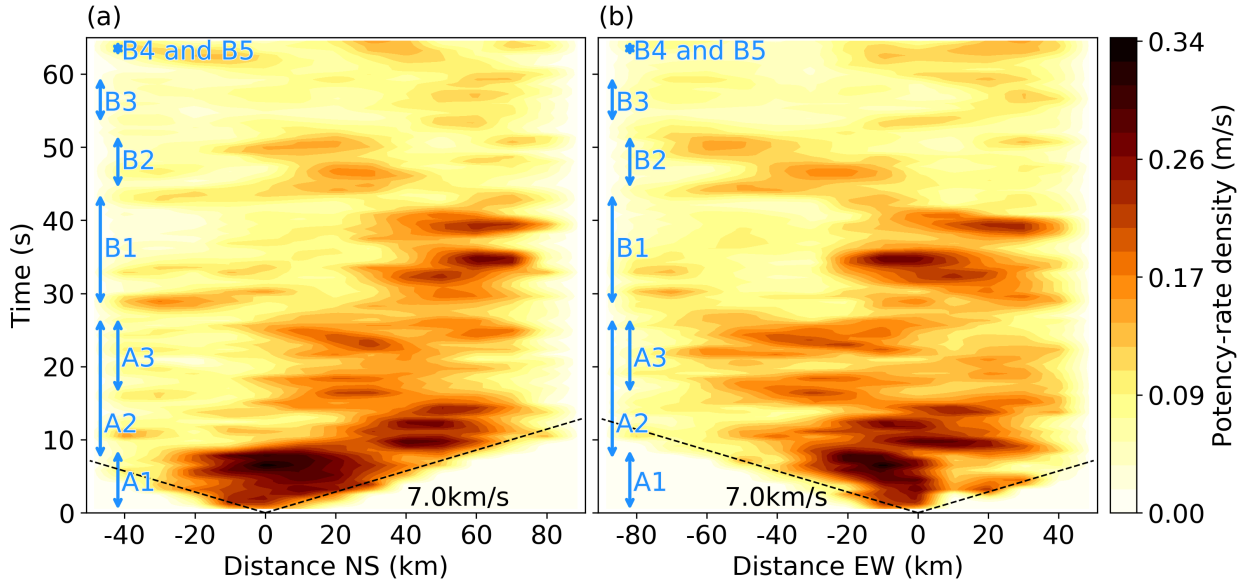

Figure 4. Time evolution of potency-rate density distribution, projected along (a) north-south and (b) east-west directions, where the positive distance directs toward (a) north and (b) east from the epicenter. North-south and east-west distances are measured along the dashed lines on the left-top panel of Fig. 3a. The dashed line represents the reference rupture speed. Each rupture phase is annotated on left of each panel. This figure was made with matplotlib (v3.1.1) [48].

Discussion

Our inversion results indicate that the main rupture stage (0–27 s after origin) affected segments oriented both N-S and E-W, suggesting that the 2018 Gulf of Alaska earthquake ruptured a conjugate fault system, as proposed in previous studies [4–8]. Our source model suggests that the rupture occurred along weak zones in the sea floor: fracture zones extending E-W and plate-bending faults parallel to N-S magnetic lineaments [29,30]. The N-S plate bending faults have been interpreted as pre-existing oceanic spreading features that were reactivated by subduction of the Pacific Plate [30]. Krabbenhoeft et al. [28] associated these pre-existing features with the radiation of high-frequency waves based on back-projection and the aftershock distribution (see Supplementary Fig. S13).

A notable irregular rupture propagation highlighted by our inversion results is the northward rupture at around 9 s in phase A1 and the southward rupture at around 12 s in phase A2, both of which stopped near the 56°N FZ (8 and 12 s, respectively, in Fig. 3a and Fig. 4a). The N-S aftershock lineation is divided into northern and southern clusters across the 56°N FZ (Fig. 3a). Given the phase A1 and A2 ruptures and the geometrical offset of the N-S aftershock lineation, the northern and southern fault system crossing the 56°N FZ can be regarded as a strike-slip step over. Based on our obtained focal mechanisms, these two N-S faults are both right-lateral strike-slip faults that dip steeply to the west (8 and 12 s in Fig. 3a), and the counterclockwise rotation of the strike angle during phase A1 is consistent with the southern N-S aftershock lineation (6 s in

Fig. 3a). Because irregular rupture behaviors are generally a result of geometric complexities, including barriers caused by discontinuous fault steps [31–33], we interpret that this fault step over caused the rupture to stagnate at around 9 and 12 s.

Multiple sub-events occurring in a conjugate strike-slip fault system have been reported in previous studies [34–38]. In this study, we have shown a causal link between the multiple rupture episodes during the 2018 Gulf of Alaska earthquake (stages A and B) and pre-existing bathymetric features by resolving both the rupture evolution and variation of fault geometry using only teleseismic body waves. Similar observations were made during the M_W 8.6 2012 Sumatra earthquake in the Wharton basin. That earthquake involved multiple $M_W > 8$ sub-events along a conjugate fault system [37,39], which developed by deep ductile shear localization beneath the brittle upper lithosphere of the oceanic plate [40].

We evaluated how the newly developed method improved the source model of the 2018 Gulf of Alaska earthquake by performing the inversion analysis with the conventional smoothness constraints [12] (Fig. S7). The inversion result with the conventional smoothness constraints show general agreement with that obtained by the improved smoothness constraints (Fig. S7). However, the spatiotemporal rupture propagation of the conventional smoothness constraints is smoother than that of the improved ones by the excessive smoothing for the most dominant $M1$ component for the earthquake (Fig. S8), which provides the blurrier image, making it difficult to clearly resolve the multiple sub-events (Figs. 3 and S7).

It is possible that the complex waveforms observed during the 2018 Gulf of Alaska earthquake were contaminated by reverberations due to the bathymetric setting that cannot be reproduced by the theoretical Green's function, resulting in dummy multiple events [41–44]. We evaluated this possibility by using empirical Green's functions [45,46] and confirm that it is unlikely that the multiple rupture stages originated from such reverberations (see Supplementary Material S3 and Fig. S10).

The sub-events that occurred after the main A1 phase can be regarded as early aftershocks missing from global catalogs [47]. Although it is difficult to distinguish whether such early near- to intermediate-field aftershocks were dynamically or statically triggered [47], it is noteworthy that the rupture propagated from A1 to A2 at more than 5 km/s (see Supplementary Material S2 and Fig. S6); this is faster than the surface wave velocity (3–4 km/s), suggesting that the A2 rupture was triggered by the A1 rupture.

Conclusions

We developed a finite-fault inversion method for teleseismic *P* waveforms with improved smoothness constraints to obtain source processes for earthquakes with complex multiple-fault ruptures. We applied our inversion method to the 2018 Gulf of Alaska earthquake and estimated its spatiotemporal rupture process. Although the observed waveforms are very complicated, reflecting the complex rupture process and fault geometry, the waveforms calculated from our source model fit well. The obtained source model suggests a complex multiple-shock sequence on a conjugate fault system, consistent with pre-existing bathymetric features. Irregular rupture stagnation about 20 km north of the epicenter may have been promoted by a fault step across a sea-floor fracture zone.

References

1. U.S. Geological Survey Earthquake Hazards Program. Advanced National Seismic System (ANSS) Comprehensive Catalog of Earthquake Events and Products. (2017) doi:10.5066/F7MS3QZH.
2. Dziewonski, A. M., Chou, T.-A. & Woodhouse, J. H. Determination of earthquake source parameters from waveform data for studies of global and regional seismicity. *J. Geophys. Res. Solid Earth* **86**, 2825–2852 (1981).
3. Ekström, G., Nettles, M. & Dziewoński, A. M. The global CMT project 2004-2010: Centroid-moment tensors for 13,017 earthquakes. *Phys. Earth Planet. Inter.* **200**–**201**, 1–9 (2012).
4. Guo, R. *et al.* The 2018 M_w 7.9 Offshore Kodiak, Alaska, Earthquake: An Unusual Outer Rise Strike-Slip Earthquake. *J. Geophys. Res. Solid Earth* **125**, (2020).
5. Hossen, M. J., Sheehan, A. F. & Satake, K. A Multi-fault Model Estimation from Tsunami Data: An Application to the 2018 M7.9 Kodiak Earthquake. *Pure Appl. Geophys.* **177**, 1335–1346 (2020).
6. Lay, T., Ye, L., Bai, Y., Cheung, K. F. & Kanamori, H. The 2018 M W 7.9 Gulf of Alaska Earthquake: Multiple Fault Rupture in the Pacific Plate. *Geophys. Res. Lett.* **45**, 9542–9551 (2018).
7. Ruppert, N. A. *et al.* Complex Faulting and Triggered Rupture During the 2018 M W 7.9 Offshore Kodiak, Alaska, Earthquake. *Geophys. Res. Lett.* **45**, 7533–7541 (2018).
8. Zhao, B. *et al.* Coseismic slip model of the 2018 M w 7.9 gulf of Alaska earthquake and its seismic hazard implications. *Seismol. Res. Lett.* **90**, 642–648 (2019).
9. Duputel, Z., Agram, P. S., Simons, M., Minson, S. E. & Beck, J. L. Accounting for prediction uncertainty when inferring subsurface fault slip. *Geophys. J. Int.* **197**, 464–482 (2014).
10. Minson, S. E., Simons, M. & Beck, J. L. Bayesian inversion for finite fault earthquake source models I—theory and algorithm. *Geophys. J. Int.* **194**, 1701–1726 (2013).
11. Ragon, T., Sladen, A. & Simons, M. Accounting for uncertain fault geometry in earthquake source inversions – I: theory and simplified application. *Geophys. J. Int.* **214**, 1174–1190 (2018).
12. Shimizu, K., Yagi, Y., Okuwaki, R. & Fukahata, Y. Development of an inversion method to extract information on fault geometry from teleseismic data. *Geophys. J. Int.* **220**, 1055–1065 (2020).
13. Yagi, Y. & Fukahata, Y. Introduction of uncertainty of Green's function into waveform inversion for seismic source processes. *Geophys. J. Int.* **186**, 711–720 (2011).
14. Das, S. & Kostrov, B. V. Inversion for seismic slip rate history and distribution with stabilizing constraints: Application to the 1986 Andreanof Islands Earthquake. *J. Geophys. Res.* **95**, 6899 (1990).
15. Hartzell, S. H. & Heaton, T. H. Inversion of strong ground motion and teleseismic waveform data for the fault rupture history of the 1979 Imperial Valley, California, earthquake. *Bull. Seismol. Soc. Am.* **73**, 1553–1583 (1983).
16. Kikuchi, M. & Kanamori, H. Inversion of complex body waves - III. *Bull. - Seismol. Soc. Am.* **81**, 2335–2350 (1991).
17. Tadapansawut, T., Okuwaki, R., Yagi, Y. & Yamashita, S. Rupture Process of the 2020 Caribbean Earthquake Along the Oriente Transform Fault, Involving Supershear Rupture and Geometric Complexity of Fault. *Geophys. Res. Lett.* **48**, 1–9 (2021).

18. Bird, P. An updated digital model of plate boundaries. *Geochemistry, Geophys. Geosystems* **4**, (2003).
19. Matthews, K. J., Mller, R. D., Wessel, P. & Whittaker, J. M. The tectonic fabric of the ocean basins. *J. Geophys. Res. Solid Earth* **116**, (2011).
20. Wessel, P. *et al.* Semiautomatic fracture zone tracking. *Geochemistry, Geophys. Geosystems* **16**, 2462–2472 (2015).
21. GEBCO Bathymetric Compilation Group 2020. GEBCO_2020 Grid. (2020) doi:10.5285/a29c5465-b138-234d- e053-6c86abc040b9.
22. Nocquet, J.-M. Stochastic static fault slip inversion from geodetic data with non-negativity and bound constraints. *Geophys. J. Int.* **214**, 366–385 (2018).
23. Yabuki, T. & Matsu'ura, M. Geodetic data inversion using a Bayesian information criterion for spatial distribution of fault slip. *Geophys. J. Int.* **109**, 363–375 (1992).
24. Wang, L., Zhao, X., Xu, W., Xie, L. & Fang, N. Coseismic slip distribution inversion with unequal weighted Laplacian smoothness constraints. *Geophys. J. Int.* **218**, 145–162 (2019).
25. Akaike, H. Likelihood and the Bayes procedure. *Trab. Estad. Y Investig. Oper.* **31**, 143–166 (1980).
26. Okuwaki, R., Yagi, Y., Aránguiz, R., González, J. & González, G. Rupture Process During the 2015 Illapel, Chile Earthquake: Zigzag-Along-Dip Rupture Episodes. *Pure Appl. Geophys.* **173**, 1011–1020 (2016).
27. Laske, G., Masters, G., Ma, Z. & Pasyanos, M. Update on CRUST1.0---A 1-degree global model of Earth's crust. *EGU Gen. Assem. 2013* **15**, 2658 (2013).
28. Krabbenhoeft, A., von Huene, R., Miller, J. J., Lange, D. & Vera, F. Strike-slip 23 January 2018 MW 7.9 Gulf of Alaska rare intraplate earthquake: Complex rupture of a fracture zone system. *Sci. Rep.* **8**, 13706 (2018).
29. Naugler, F. P. & Wageman, J. M. Gulf of Alaska: Magnetic anomalies, fracture zones, and plate interaction. *Bull. Geol. Soc. Am.* **84**, 1575–1584 (1973).
30. Reece, R. S. *et al.* The role of farfield tectonic stress in oceanic intraplate deformation, Gulf of Alaska. *J. Geophys. Res. Solid Earth* **118**, 1862–1872 (2013).
31. Aki, K. Characterization of barriers on an earthquake fault. *J. Geophys. Res.* **84**, 6140–6148 (1979).
32. Das, S. & Aki, K. Fault plane with barriers: A versatile earthquake model. *J. Geophys. Res.* **82**, 5658–5670 (1977).
33. Harris, R. A. & Day, S. M. Dynamics of fault interaction: parallel strike-slip faults. *J. Geophys. Res.* **98**, 4461–4472 (1993).
34. Fukuyama, E. Dynamic faulting on a conjugate fault system detected by near-fault tilt measurements. *Earth, Planets Sp.* **67**, 38 (2015).
35. Goldberg, D. E. *et al.* Complex Rupture of an Immature Fault Zone: A Simultaneous Kinematic Model of the 2019 Ridgecrest, CA Earthquakes. *Geophys. Res. Lett.* **47**, (2020).
36. Hudnut, K. *et al.* Surface ruptures on cross-faults in the 24 November 1987 Superstition Hills, California, earthquake sequence. *Bull. Seismol. Soc. Am.* **79**, 282–296 (1989).
37. Meng, L. *et al.* Earthquake in a maze: Compressional rupture branching during the 2012 Mw 8.6 Sumatra earthquake. *Science (80-.).* **337**, 724–726 (2012).
38. Ross, Z. E. *et al.* Hierarchical interlocked orthogonal faulting in the 2019 Ridgecrest earthquake sequence. *Science (80-.).* **366**, 346–351 (2019).

39. Duputel, Z. *et al.* The 2012 Sumatra great earthquake sequence. *Earth Planet. Sci. Lett.* **351**–**352**, 247–257 (2012).
40. Liang, C., Ampuero, J.-P. & Muñoz, D. P. Deep ductile shear zone facilitates near-orthogonal strike-slip faulting in a thin brittle lithosphere. *Geophys. Res. Lett.* **n/a**, e2020GL090744 (2020).
41. Fan, W. & Shearer, P. M. Coherent Seismic Arrivals in the *P* Wave Coda of the 2012 M_w 7.2 Sumatra Earthquake: Water Reverberations or an Early Aftershock? *J. Geophys. Res. Solid Earth* **123**, 3147–3159 (2018).
42. Wiens, D. A. Effects of near source bathymetry on teleseismic P waveforms. *Geophys. Res. Lett.* **14**, 761–764 (1987).
43. Wiens, D. A. Bathymetric effects on body waveforms from shallow subduction zone earthquakes and application to seismic processes in the Kurile Trench. *J. Geophys. Res. Solid Earth* **94**, 2955–2972 (1989).
44. Yue, H., Castellanos, J. C., Yu, C., Meng, L. & Zhan, Z. Localized water reverberation phases and its impact on backprojection images. *Geophys. Res. Lett.* **44**, 9573–9580 (2017).
45. Dreger, D. S. Empirical Green's function study of the January 17, 1994 Northridge, California earthquake. *Geophys. Res. Lett.* **21**, 2633–2636 (1994).
46. Hartzell, S. H. Earthquake aftershocks as Green's functions. *Geophys. Res. Lett.* **5**, 1–4 (1978).
47. Fan, W. & Shearer, P. M. Local near instantaneously dynamically triggered aftershocks of large earthquakes. *Science (80-.).* **353**, 1133–1136 (2016).
48. Hunter, J. D. Matplotlib: A 2D graphics environment. *Comput. Sci. Eng.* **9**, 90–95 (2007).
49. Beyreuther, M. *et al.* ObsPy: A python toolbox for seismology. *Seismol. Res. Lett.* **81**, 530–533 (2010).
50. Wessel, P., Smith, W. H. F., Scharroo, R., Luis, J. & Wobbe, F. Generic mapping tools: Improved version released. *Eos (Washington. DC).* **94**, 409–410 (2013).

Acknowledgments

We thank the editor and the reviewers for evaluating the manuscript. This work was supported by the Grant-in-Aid for Scientific Research (C) 19K04030. The facilities of IRIS Data Services, and specifically the IRIS Data Management Center, were used for access to waveforms, related metadata, and/or derived products used in this study. IRIS Data Services are funded through the Seismological Facilities for the Advancement of Geoscience (SAGE) Award of the National Science Foundation under Cooperative Support Agreement EAR-1851048. We are grateful to Dr. Anne Krabbenhöft and Dr. Felipe Vera for providing us with their back-projection image [28]. All the figures were generated with matplotlib (v3.1.1: https://doi.org/10.5281/zenodo.3264781) [48], ObsPy (v1.1.0: https://doi.org/10.5281/zenodo.165135) [49]and Generic Mapping Tools (v5.4.5) [50].

Author contributions

S.Y. and Y.Y. conceptualized this study, compiled the data and conducted the analyses. S.Y., Y.Y., R.O., K.S, R.A. and Y.F. contributed to the methodology. S.Y., Y.Y., R.O. and K.S. processed and interpreted the data. S.Y. and Y.Y. wrote the manuscript which was revised and edited by R.O., K.S., R.A. and Y.F. All authors approved the submitted manuscript. All authors agreed both to be personally accountable for the author's own contributions and to ensure that questions related to

the accuracy or integrity of any part of the work, even ones in which the author was not personally involved, are appropriately investigated, resolved, and the resolution documented in the literature.

Additional information

Correspondence and requests for materials should be addressed to S.Y. or Y.Y.

Data Availability

Waveform data was downloaded through the IRIS Wilber 3 system (https://ds.iris.edu/wilber3/find_stations/10607586). Teleseismic waveforms were obtained from the following networks: the Canadian National Seismograph Network (CN; https://doi.org/10.7914/SN/CN); the Caribbean USGS Network (CU; https://doi.org/10.7914/SN/CU); the GEOSCOPE (G; https://doi.org/10.18715/GEOSCOPE.G); the Hong Kong Seismograph Network (HK; https://www.fdsn.org/networks/detail/HK/); the New China Digital Seismograph Network (IC; https://doi.org/10.7914/SN/IC); the IRIS/IDA Seismic Network (II; https://doi.org/10.7914/SN/II); the International Miscellaneous Stations (IM; https://www.fdsn.org/networks/detail/IM/); the Global Seismograph Network (IU; https://doi.org/10.7914/SN/IU), and the Pacific21 (PS; https://www.fdsn.org/networks/detail/PS/). The moment tensor solutions are obtained from the GCMT catalog (https://www.globalcmt.org/CMTsearch.html). The CRUST 1.0 model is available at https://igppweb.ucsd.edu/~gabi/crust1.html. The fracture zone data is obtained from the Global Seafloor Fabric and Magnetic Lineation Data Base Project website (http://www.soest.hawaii.edu/PT/GSFML/).

Supporting Information for

Consecutive Ruptures on a Complex Conjugate Fault System During the 2018 Gulf of Alaska Earthquake

Shinji Yamashita[1, *], Yuji Yagi[2, **], Ryo Okuwaki[2, 3, 4], Kousuke Shimizu[1], Ryoichiro Agata[4], and Yukitoshi Fukahata[5]

[1]Graduate School of Life and Environmental Sciences, University of Tsukuba, Tsukuba, Ibaraki 305-8572, Japan
[2]Faculty of Life and Environmental Sciences, University of Tsukuba, Tsukuba, Ibaraki 305-8572, Japan
[3]Mountain Science Center, University of Tsukuba, Ibaraki 305-8572, Japan
[4]COMET, School of Earth and Environment, University of Leeds, Leeds LS2 9JT, UK
[5]Japan Agency for Marine-Earth Science and Technology, 3173-25 Showa-machi, Kanazawa-ku, Yokohama 236-0001, Japan
[6]Disaster Prevention Research Institute, Kyoto University, Uji, Kyoto 611-0011, Japan
[*]Corresponding author: Shinji Yamashita (syamashita@geol.tsukuba.ac.jp)
[**]Second corresponding author: Yuji Yagi (yagi-y@geol.tsukuba.ac.jp)

Contents of this file

Introduction

This Supporting Information contains numerical tests for validation of the developed finite-fault inversion method (Material S1, Figs. S1 to S4, and Table S1). Sensitivity of the finite-fault inversion to assumptions of model planar depth and rupture velocity is shown in Material S2, and Figs. S5 and S6. Comparison with the conventional smoothness constraints is shown in Figs. S7 and S8. Results of a numerical test using our solution of the 2018 Gulf of Alaska earthquake as input data are shown in Fig. S9. The possibility of dummy imaging of reverberations is evaluated in Material S3 and Fig. S10. Waveform fits and full snapshots of the rupture evolution for our main result are shown in Figs. S11 and S12. Fig. S13 shows a comparison between our source model and the back-projection result obtained by Krabbenhoeft et al. (2018). Table S2 shows the near-filed velocity structure used for calculating Green's function. Table S3 provides the set of smoothness constraints adopted for the main result.

Note

Numerical experiment (S1)

We perform the numerical tests to evaluate effects of the improved smoothness constraints and the horizontal non-rectangular model plane. To generate synthetic waveforms, orthogonal three faults were assumed (Fig. S1a). Then, we assume the pure strike-slip rupture which spherically spread from a hypocenter at a depth of 30 km on the central fault, named F2, with a rupture velocity of 3.0 km/s (Fig. S1a and b). The moment rate function of input model has peaks at 9 and 23 s (Fig. S1c). We add a random Gaussian noise to the calculated Green's function, for which the standard deviation is 5% of maximum amplitude of each calculated Green's function. We also add a random Gaussian noise with zero mean and a standard deviation of 1.0 μm as background noise. We generate the synthetic waveforms at 78 stations used in the inversion of the 2018 Gulf of Alaska earthquake (Fig. 2c).

We compare results of four cases: (1) the rectangular model plane and the conventional smoothness constraints; (2) the rectangular model plane and the improved smoothness constraints; (3) the non-rectangular model plane and the conventional smoothness constraints, and (4) the non-rectangular model plane and the improved smoothness constraints.

We set the horizontal rectangular model plane with a width and length of 120 km to cover the input three faults (Fig. S2a). The depth of the model plane is set to 30 km, which corresponds to the centroid depth of input source model. The spatial knot interval is set to 10 km. For the cases (3) and (4), we design the non-rectangular model plane based on the input three faults (Fig. S2d). For all cases, the potency-rate density function at each knot is represented as a linear combination of B-spline functions over a duration of 30 s with an interval of 0.8 s and the rupture front velocity set at 7.0 km/s. We adopt the improved smoothness constraints at the cases (2) and (4) by referring to the input focal mechanism (Table S1).

In the case (1), the resultant moment rate function is smoother than the input one and has only one peak at 12 s, which is about 3 s later than the first peak of the input (Fig. S2b). The normalized L2 norm, which represents the degree of misfit between the input and the resultant moment rate function (hereinafter called "the L2 norm" for simplicity), was 0.245. The snapshots show a wider potency-rate density distribution than the input, making it difficult to identify the fault geometry and interpret the source process (Fig. S3a and b). Figure S4 shows the self-normalized potency-rate function for each basis component, obtained by taking a spatial integration of the potency-rate density function for each basis component. In the case (1), the potency-rate function of $M1$ component (Kikuchi & Kanamori, 1991), corresponding to the input slip direction, is smoother than those of other components (Fig. S4). This is because the conventional smoothness constraints work to excessively smooth out the dominant basis components.

In the case (2), the moment rate function yields two peaks at 10 and 23 s, which close to the input peaks (Fig. S2c). The L2 norm is 0.074. The improved smoothness constraints remove the bias in the resultant potency-rate function of the $M1$ component (Fig. S4) and thus the spatiotemporal potency-rate density distribution of the case (2) is

finer than that of the case (1) (Fig. S3c). However, in the case (2), the image looks too blurry to resolve two independent ruptures of the input model due to insufficient spatial resolution (snapshot at 15 and 20 s in Fig. S3c).

In the case (3), the moment rate function has two peaks at 11 and 23 s, which close to the input peaks (Fig. S2e). The L2 norm is 0.135 and slightly larger than the case (2). The potency-rate density distribution of the case (3) at 15 and 20 s resolves two ruptures, which are not well resolved in the case (2) (15 and 20 s in Fig. S3d). The spatial resolution of the inversion results is improved because the model space modification according to the input fault geometry is identical to implicitly introducing *a priori* constraint of the fault geometry (e.g., aftershock distribution). The model space reduction also contributes to reduce computational costs, which is useful for analyses of earthquakes having a vast source area, such as the 2018 Gulf of Alaska earthquake.

In the case (4), the moment rate function reproduces the input in detail (Fig. S2f), and the rupture evolution is fine enough to reproduce the input (Fig. S3e). The L2 norm of the case (4) is 0.071, which is the minimum value among the four cases. Thus, we conclude from our numerical tests that the optimum strategy should be by using both the improved smoothness constraints and the horizontal non-rectangular model plane.

Sensitivity test (S2)

We evaluate the sensitivity of the inversion results by perturbating the model parameters. We perform the inversion analyses by changing the model plane depth to 33.6$\pm$5 km. The obtained snapshots show the rupture pattern is insensitive to the model planar depths (Fig. S5). We also check the inversion results by changing the assumption of maximum rupture velocity to 3 and 5 km/s. We resolve the similar rupture processes for the maximum rupture velocities at 5 and 7 km/s (Fig. S6b and c). However, when assuming 3 km/s, the model does not clearly show the A2 rupture (Fig. S6a). This is due to the limited model space that could artificially vanish the possible slip behavior beyond the designated rupture front.

Verification of using empirical Green's functions (S3)

As shown in Figs. 2 and S11, our finite-fault model sufficiently reproduces the complicated observed teleseismic *P* waves, resulting in showing the complex-multiple rupture episodes. On the other hand, pulses of the observed waveforms may include later arrivals due to structure complexities in the source region (e.g., Fan & Shearer, 2018; Yue et al., 2017). However, the theoretical Green's functions, assuming a 1D-layered structure model, are often poorly modeled for reverberations of dipping near-source bathymetry (Wiens 1987, 1989), which may induce artificial imaging of multiple-shock sequence. In principle, seismograms of relatively smaller earthquakes with a similar focal mechanism that occurred near the target earthquake can be regarded as an empirical Green's function (EGF) under an assumption that the moment rate function of that small earthquake is simple and short (Hartzell 1978; Dreger 1994). We here employ the EGFs instead of the theoretical Green's functions to evaluate whether multiple-shock sequence that we resolve is likely from the source effect or the reverberations. We deconvolve the EGFs from the

observed waveforms of the 2018 Gulf of Alaska earthquake for each station to remove the effects of the earth response including possible reverberations.

We select three events from the GCMT catalog (Dziewonski et al., 1981; Ekström et al., 2012) as the EGFs with the clear first *P*-phase motion and high signal-to-noise ratios (Fig. S10a). The EGFs and the mainshock data are band-passed between 0.01 and 2 Hz and converted into ground velocities with a sampling interval of 0.1 s. We solve the least squares problem using the non-negative least squares algorithm of Lawson and Hanson (1974). We perform deconvolution for both a maximum source duration of 65 and 27 s to evaluate the validity of the sub-events resolved after 27 s for the mainshock (Fig. S10b, c, d, and e).

The normalized moment rate functions obtained in the maximum length of 65 s show non-negligible moment release even after 27 s (Fig. S10b, c, d and e). If the subevents after 27 s were artifacts caused by the reverberations of the initial rupture, the observed waveforms would be reproducible by convolving the moment rate function up to 27 s with the EGF. However, the synthesized waveforms obtained from the 27-s-moment-rate function fails to reproduce the several pulses of the observed waveforms, while the synthesized waveforms obtained from the 65-s-moment-rate function better fits the observed waveforms, suggesting that the subevents after 27 s should be necessary to explain the observed data (Fig. S10b, c, d and e).

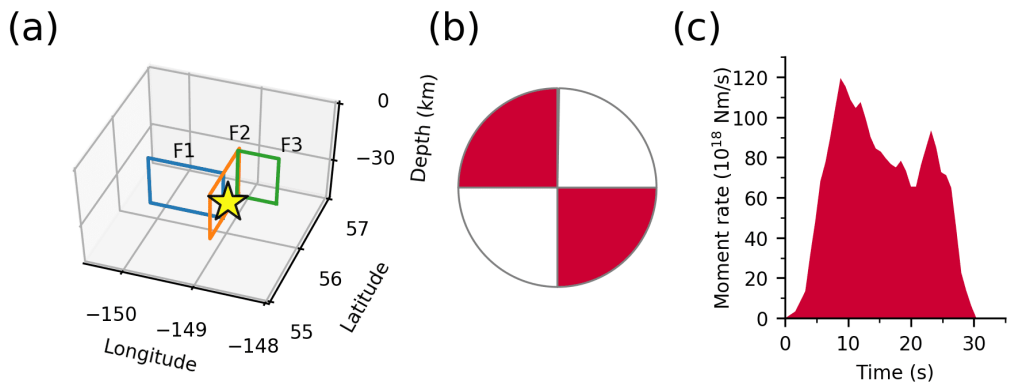

Figure S1. Input source model for the numerical tests. (a) Input fault geometry. The star indicates the location of the initial break. All three faults have dips of 90° and down-dip widths of 25 km. F1 (Blue) has a strike of 90° and a length of 65 km. F2 (Orange) has a strike of 0° and a length of 100 km. F3 (Green) has a strike of 90° and a length of 35 km. (b) Total focal mechanism of the input slip-rate. (c) Input moment rate function. This figure was made with matplotlib (v3.1.1; Hunter, 2007) and ObsPy (v1.1.0; Beyreuther et al., 2010).

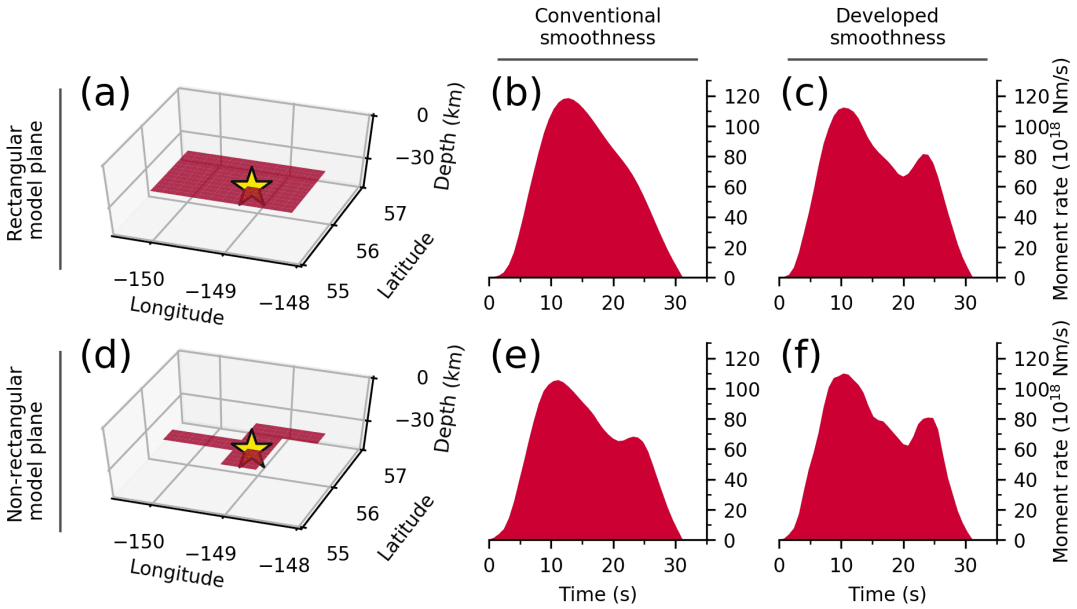

Figure S2. Assumed model planes and resultant moment rate functions for the numerical tests. (a) and (d) represent the rectangular model plane and the non-rectangular model plane, respectively. (b), (c), (e) and (f) show the moment rate functions obtained by the rectangular model plane and the conventional smoothness constraints (case 1), the rectangular model plane and the improved smoothness constraints (case 2), the non-rectangular model plane and the conventional smoothness constraints (case 3), and the non-rectangular model plane and the improved smoothness constraints (case 4), respectively. This figure was made with matplotlib (v3.1.1; Hunter, 2007).

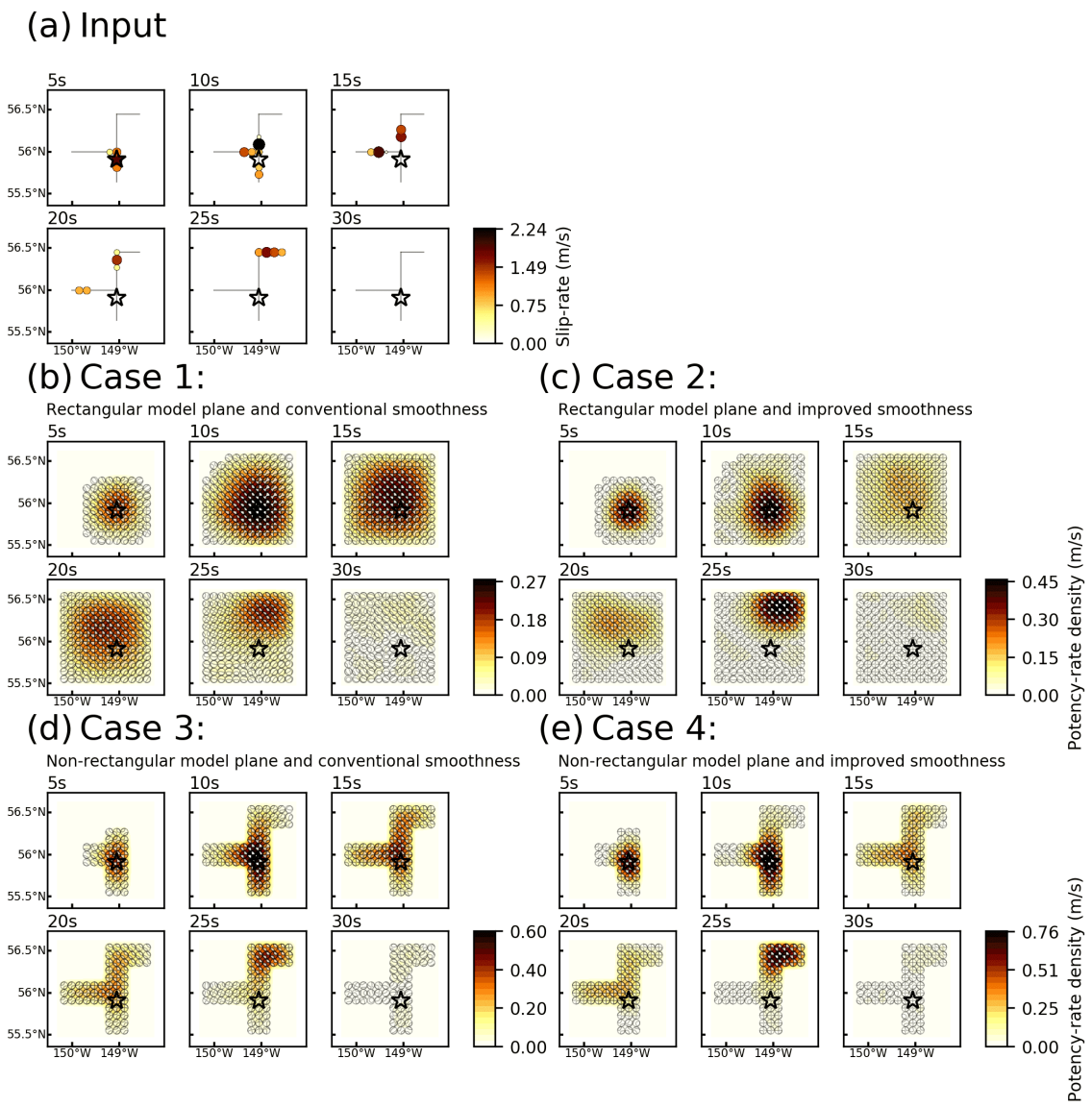

Figure S3. Snapshots of (a) input slip-rate and (b) to (e) resultant potency-rate density tensors for each numerical-test case every 5 s. The star denotes the initial breaking point. The dots in panel (a) denote the input source positions. Color of these dots represents the value of slip-rate. The gray line in panel (a) represents the input fault geometry. This figure was made with matplotlib (v3.1.1; Hunter, 2007) and ObsPy (v1.1.0; Beyreuther et al., 2010).

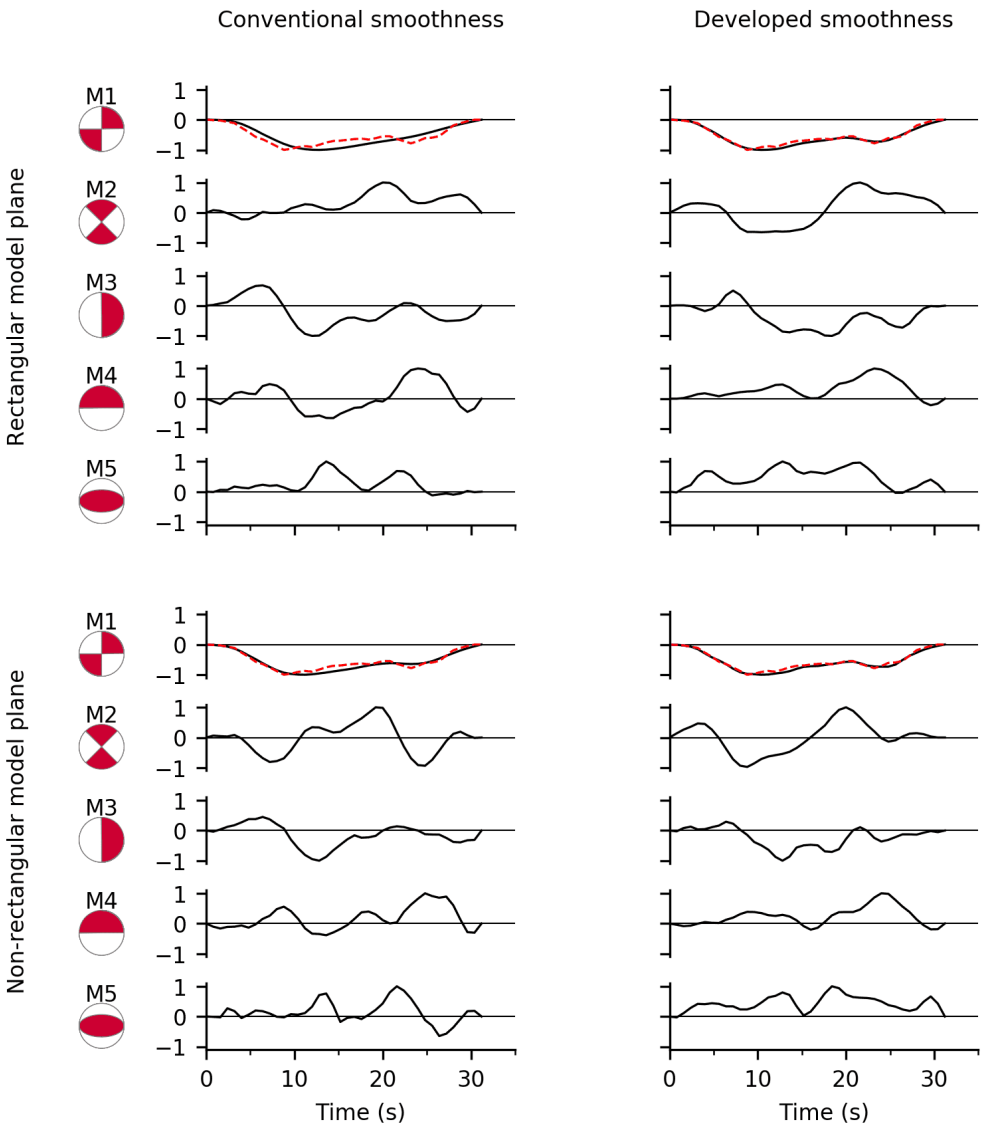

Figure S4. Comparison of the input slip-rate function (dashed line) and the potency-rate functions for each basis component, obtained by taking a spatial integration of the potency-rate density function (Kikuchi & Kanamori, 1991) (solid line). Each trace is self-normalized. This figure was made with matplotlib (v3.1.1; Hunter, 2007) and ObsPy (v1.1.0; Beyreuther et al., 2010).

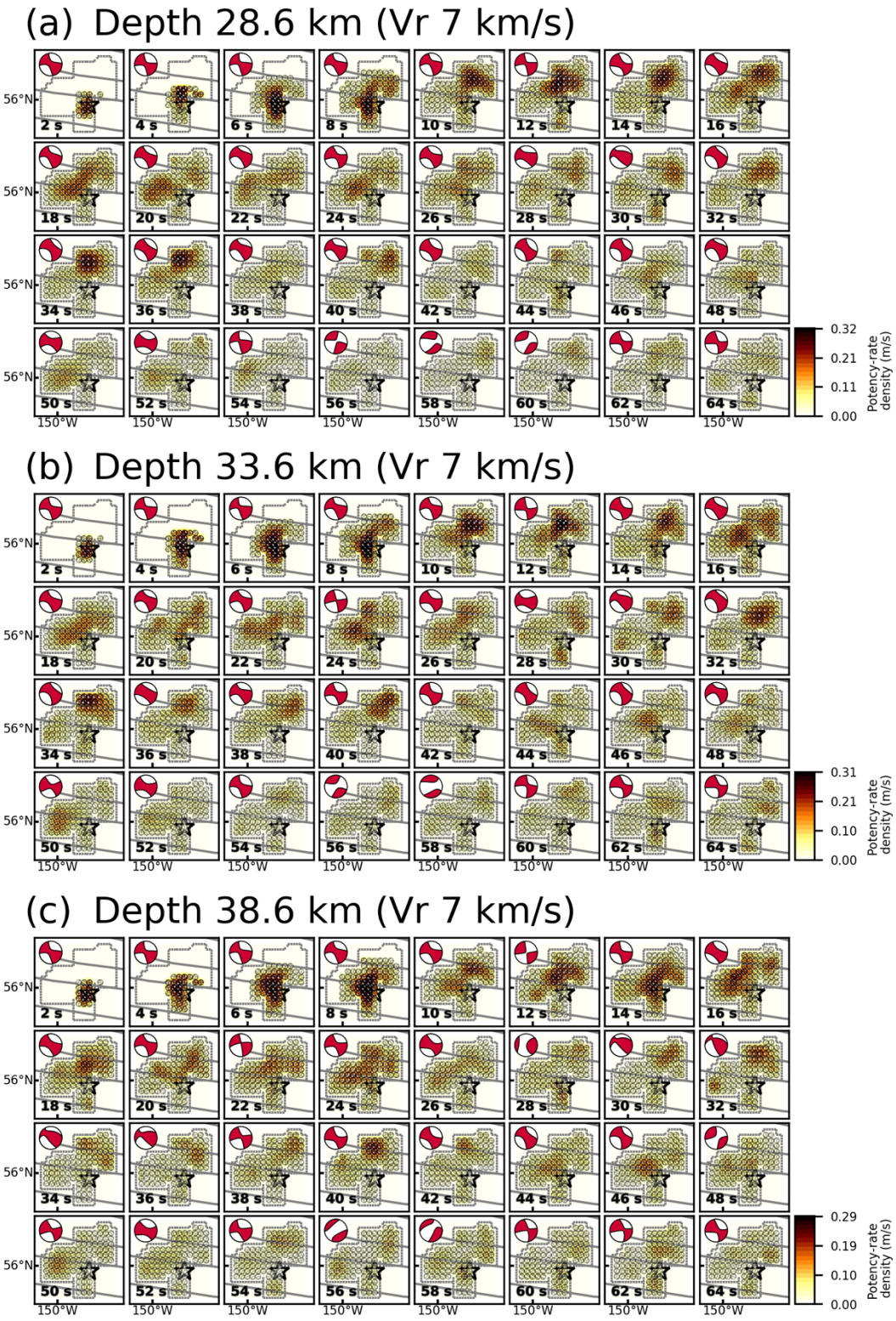

Figure S5. Summary of snapshots of the potency-rate density tensors for the different assumptions of model plane depth for the 2018 Gulf of Alaska earthquake. The depth of each snapshot is (a) 28.6 km, (b) 33.6 km, and (c) 38.6 km. The rupture front velocity (Vr) is

7 km/s for all the snapshots. The corresponding time after onset for each snapshot is noted at the bottom-left of each panel. The dotted line shows the border of the assumed model plane. The star and solid lines indicate the epicenter (AEC) and the fracture zones (Matthews et al, 2011; Wessel et al., 2015), respectively. The large beachball in each panel indicates the corresponding total moment tensor at each time. This figure was made with matplotlib (v3.1.1; Hunter, 2007) and ObsPy (v1.1.0; Beyreuther et al., 2010).

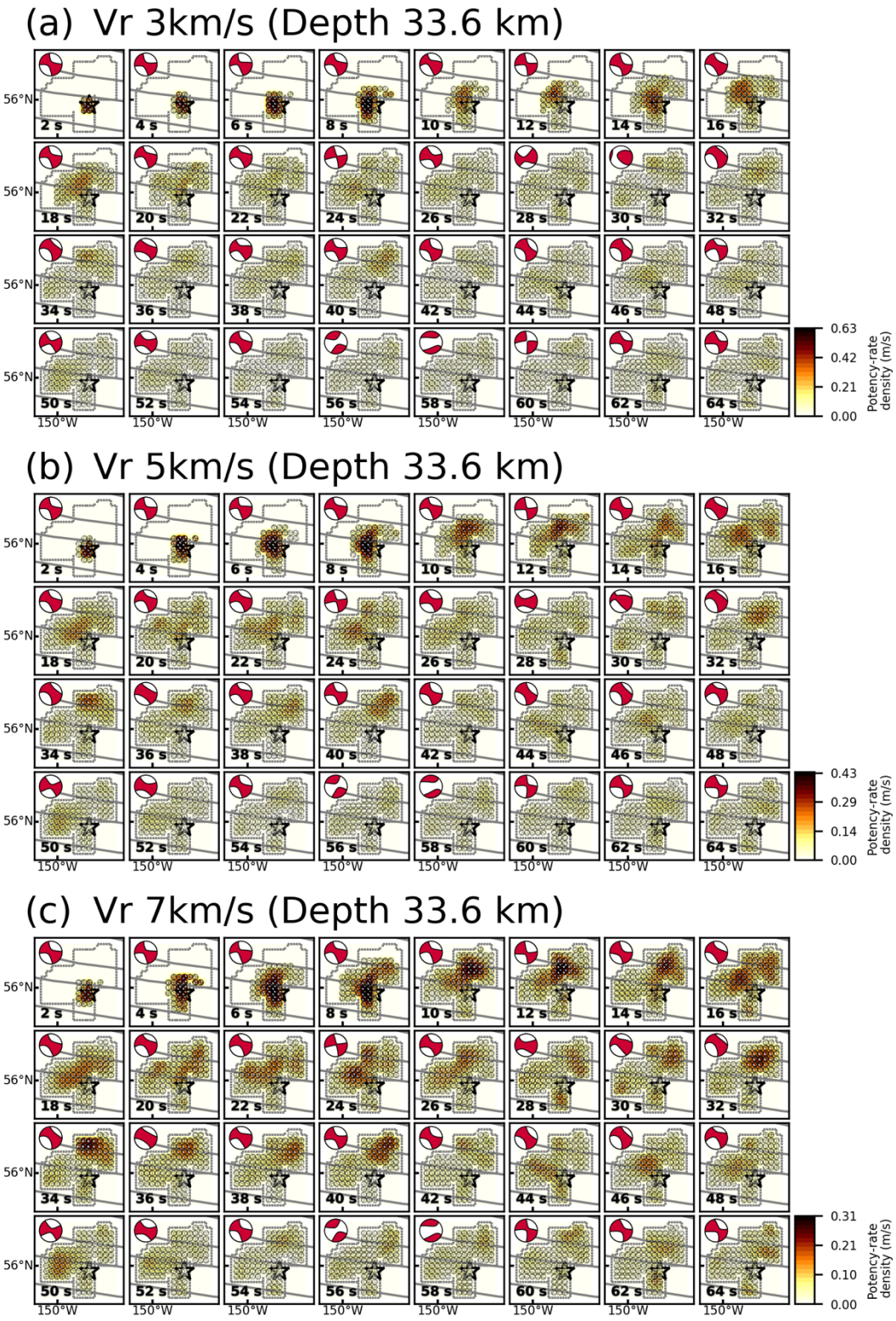

Figure S6. Summary of snapshots of the potency-rate density tensors for the different assumptions of rupture front velocity (Vr) for the 2018 Gulf of Alaska earthquake. The rupture front velocity of each snapshot is (a) 3 km/s, (b) 5 km/s, and (c) 7 km/s. The model

plane depth is 33.6 km for all the snapshots. This figure was made with matplotlib (v3.1.1; Hunter, 2007) and ObsPy (v1.1.0; Beyreuther et al., 2010).

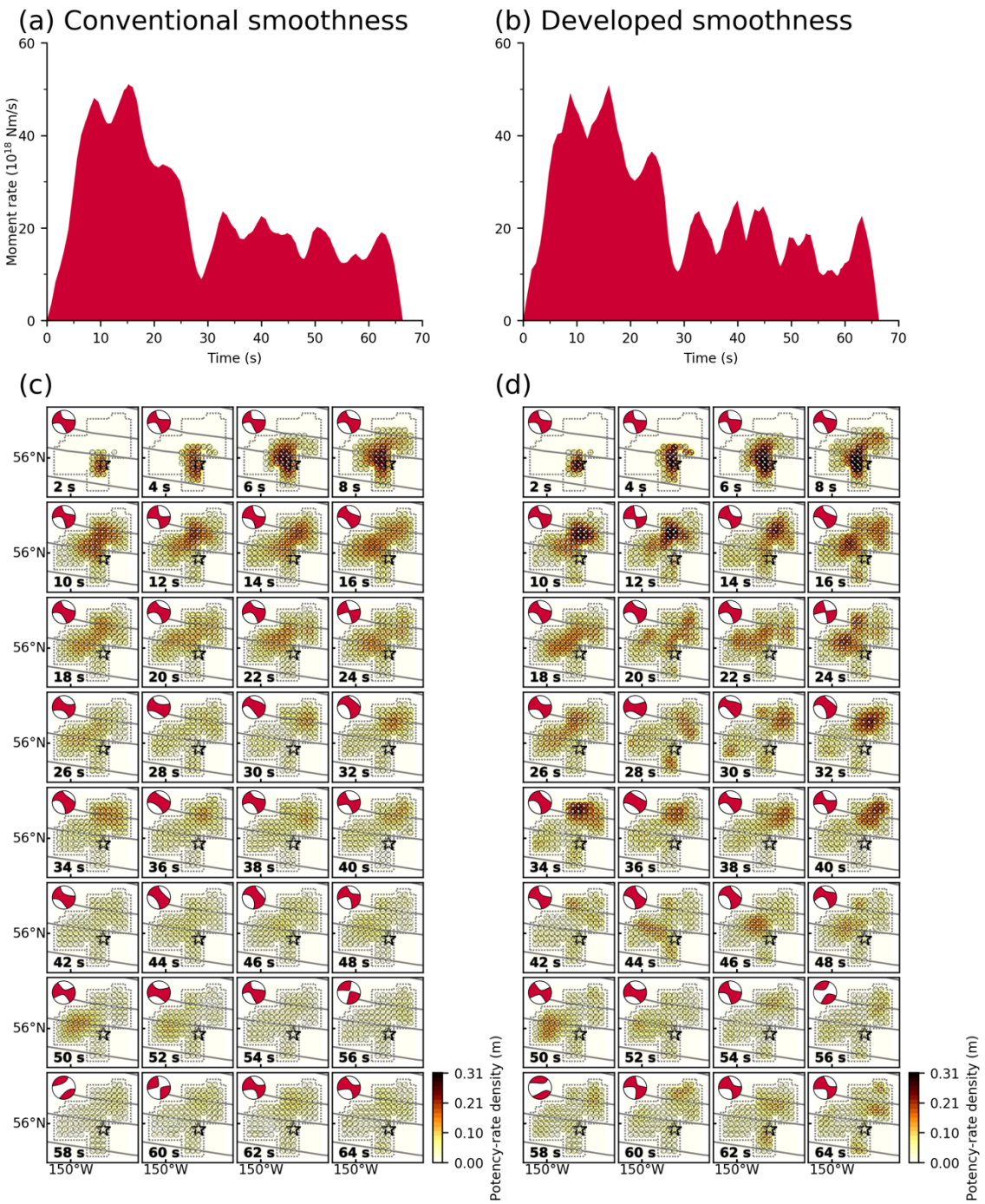

Figure S7. Comparison of results obtained by the conventional and developed smoothness constraints for the 2018 Gulf of Alaska earthquake. (a) and (b) show the moment rate functions obtained by the conventional and developed smoothness constraints, respectively. (c) and (d) show the snapshots obtained by the conventional and developed smoothness constraints, respectively. The corresponding time after onset for each snapshot is noted at the bottom-left of each panel. The dotted line shows the border

of the assumed model plane. The star and solid lines indicate the epicenter (AEC) and the fracture zones (Matthews et al, 2011; Wessel et al., 2015), respectively. The large beachball in each panel indicates the corresponding total moment tensor at each time. This figure was made with matplotlib (v3.1.1; Hunter, 2007) and ObsPy (v1.1.0; Beyreuther et al., 2010).

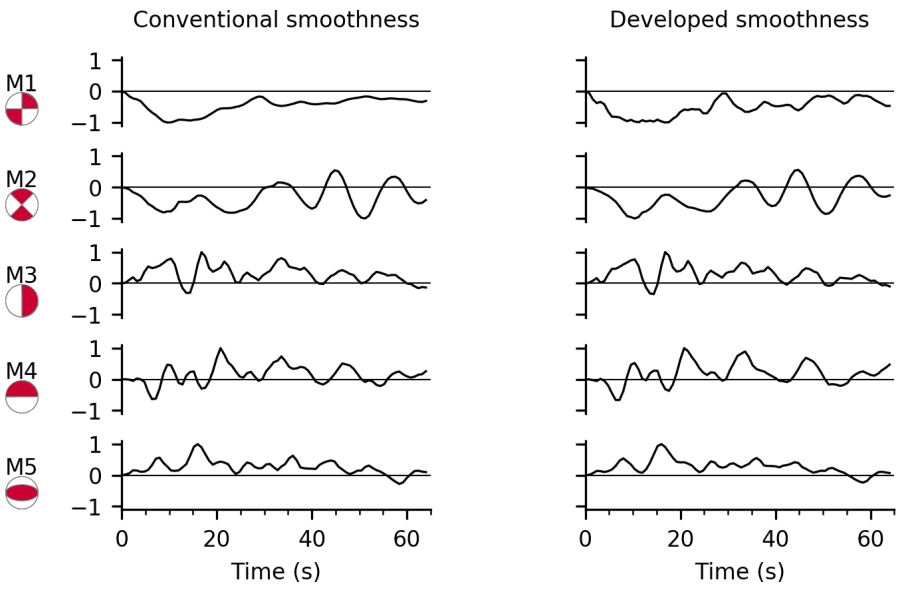

Figure S8. Comparison of the potency-rate functions of the 2018 Gulf of Alaska earthquake obtained by the conventional (left column) and improved smoothness constraints (right column) for each basis double-couple component (Kikuchi & Kanamori, 1991). Each trace is self-normalized. This figure was made with matplotlib (v3.1.1; Hunter, 2007) and ObsPy (v1.1.0; Beyreuther et al., 2010).

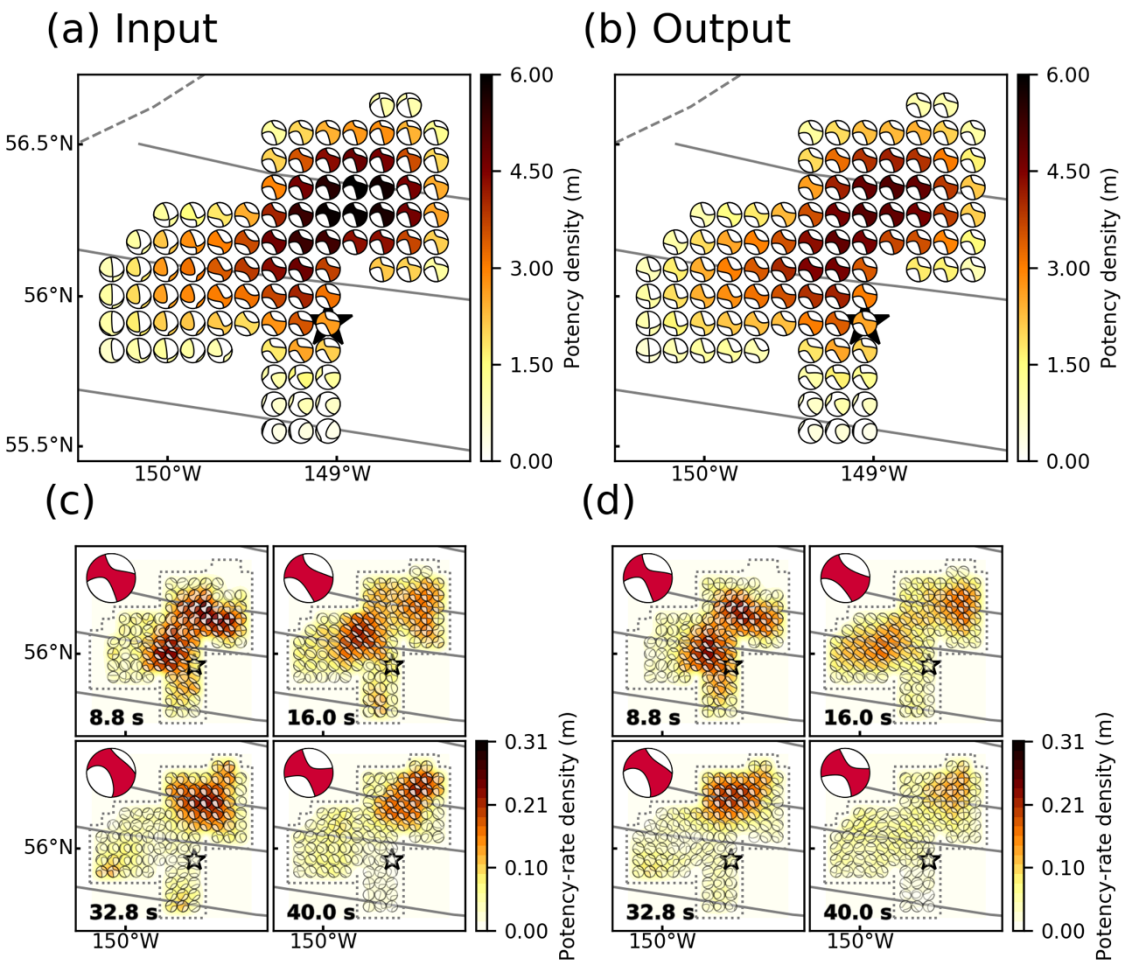

Figure S9. Sensitivity test by using the solution of the 2018 Gulf of Alaska earthquake. We inverted the synthetic waveforms of the source model (input model, Fig. 3) and evaluated the reproducibility. (a) and (b) show the potency density tensor distributions of the input and output (inversion result), respectively. (c) and (d) show the snapshots of the input and output, respectively. The hypocentral time when the snapshot is taken is on left bottom. Inset is the total moment tensor for each time. The star indicates the epicenter (AEC). The dotted line shows the border of the assumed model plane. Dashed and solid lines represent the plate boundaries (Bird, 2003) and the fracture zones (Matthews et al, 2011; Wessel et al., 2015), respectively. This figure was made with matplotlib (v3.1.1; Hunter, 2007) and ObsPy (v1.1.0; Beyreuther et al., 2010).

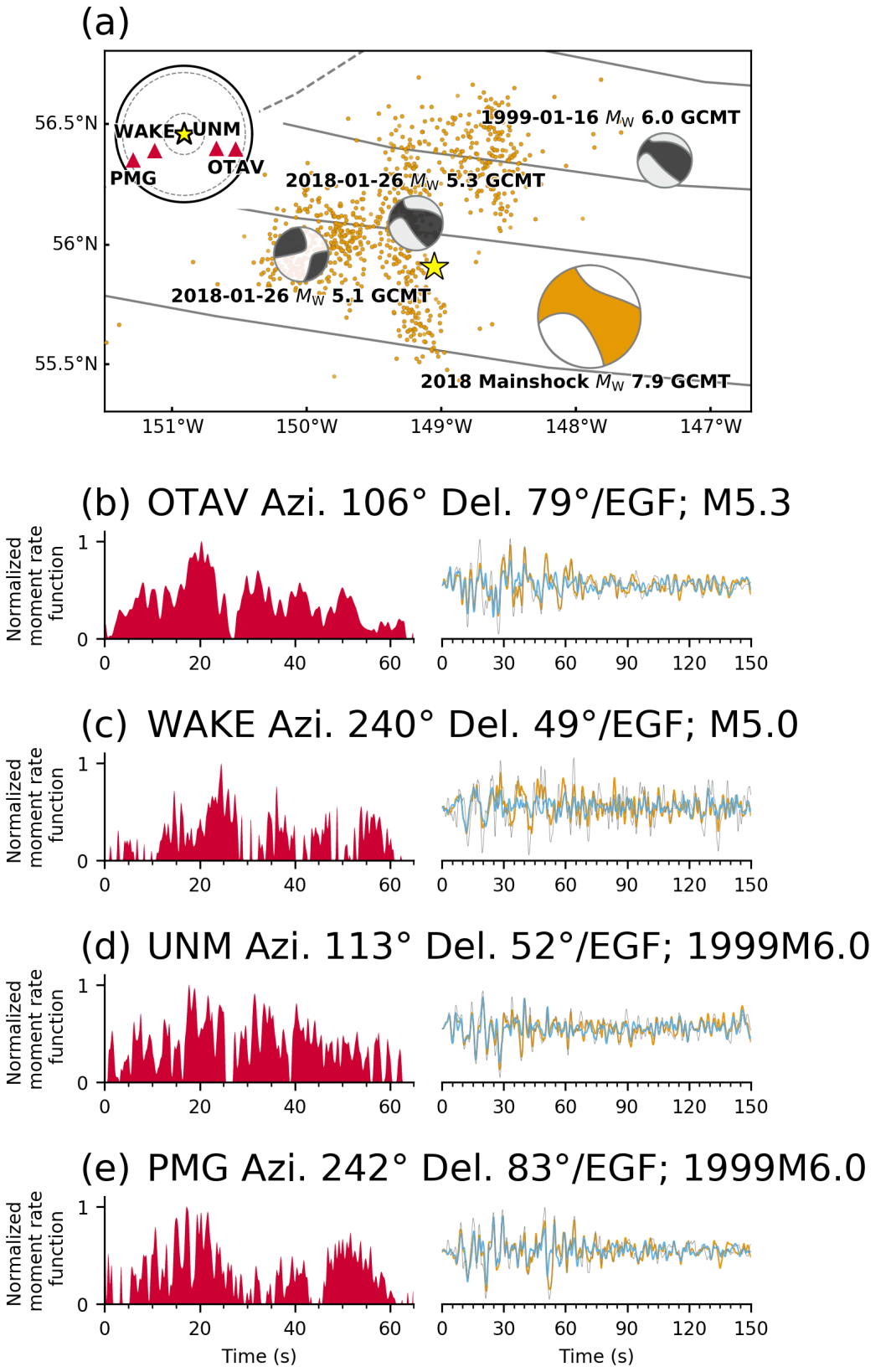
(a)
56.5°N
56°N
55.5°N
151°W
150°W
149°W
148°W
147°W
WAKE
UNM
PMG
OTAV
1999-01-16 M_W 6.0 GCMT
2018-01-26 M_W 5.3 GCMT
2018-01-26 M_W 5.1 GCMT
2018 Mainshock M_W 7.9 GCMT
(b) OTAV Azi. 106° Del. 79°/EGF; M5.3
(c) WAKE Azi. 240° Del. 49°/EGF; M5.0
(d) UNM Azi. 113° Del. 52°/EGF; 1999M6.0
(e) PMG Azi. 242° Del. 83°/EGF; 1999M6.0
Normalized moment rate function
Time (s)
Time (s)

Figure S10. Summary of the EGF analysis. (a) Map projection of the GCMT solutions of the main shock (orange beachball) and events used as the EGFs (black beachballs). The star is the mainshock epicenter, and orange dots are aftershocks ($M \geq 3$) that occurred within one week of the mainshock; all epicentral locations are from AEC. Dashed and solid lines represent the plate boundaries (Bird, 2003) and the fracture zones (Matthews et al, 2011; Wessel et al., 2015), respectively. Inset is an azimuthal equidistant projection of the station distribution. (b) to (e) show the normalized moment rate function (left) and waveform fittings (right). Gray trace is the observed waveform. Also shown are the synthetic waveforms obtained by using 65-s-moment-rate function (orange) and 27-s-moment-rate function (blue). Each panel is labeled with the station name, azimuth (Azi.) and epicentral distance (Del.) from the mainshock, and the event name used as the EGF. This figure was made with matplotlib (v3.1.1; Hunter, 2007) and ObsPy (v1.1.0; Beyreuther et al., 2010).

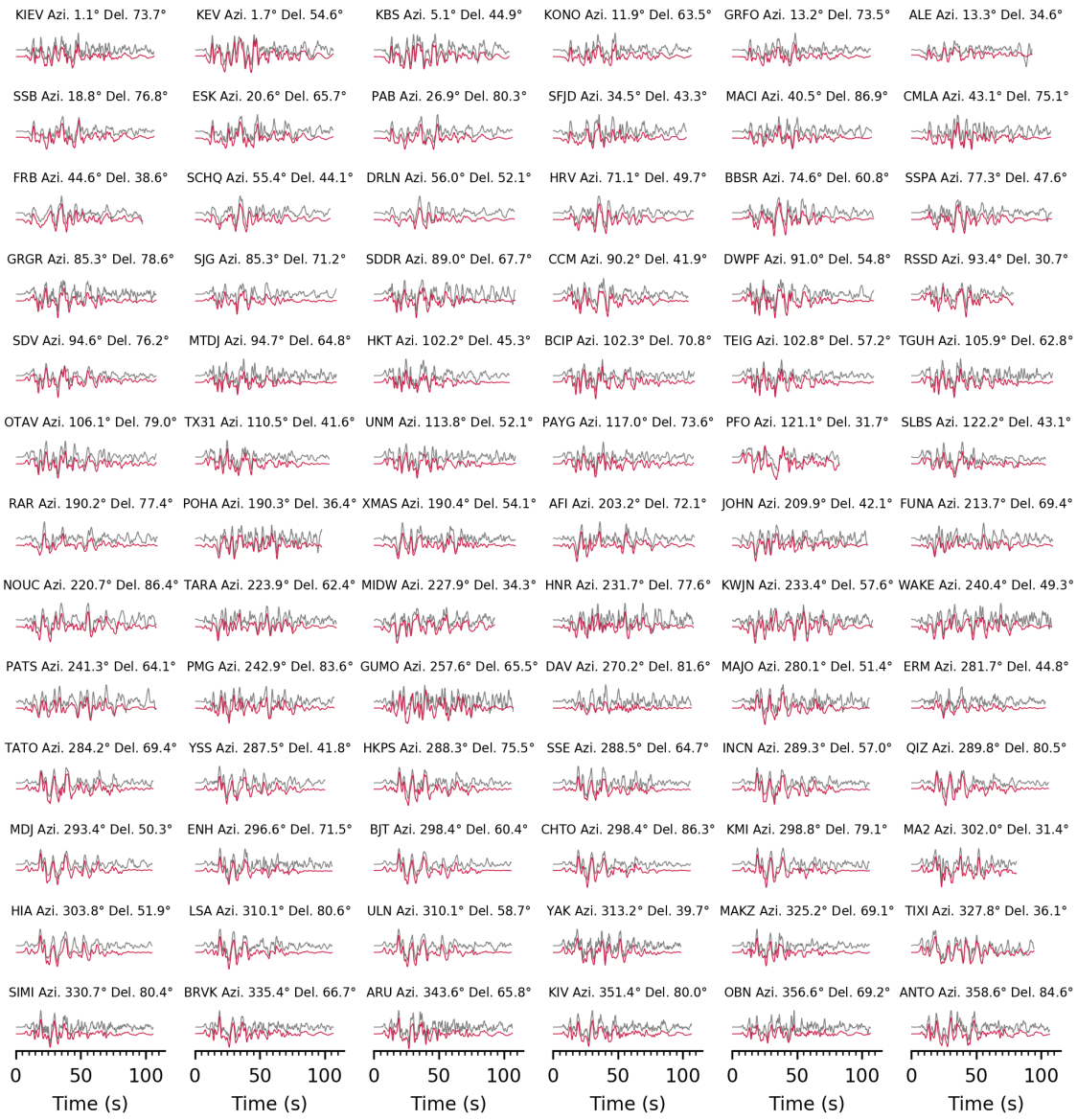

Figure S11. Comparison of observed waveforms (gray) with synthetic waveforms (red) for the main inversion results of the 2018 Gulf of Alaska earthquake. Each panel is labeled with the station name, azimuth (Azi.), and epicentral distance (Del.) from the mainshock. This figure was made with matplotlib (v3.1.1; Hunter, 2007).

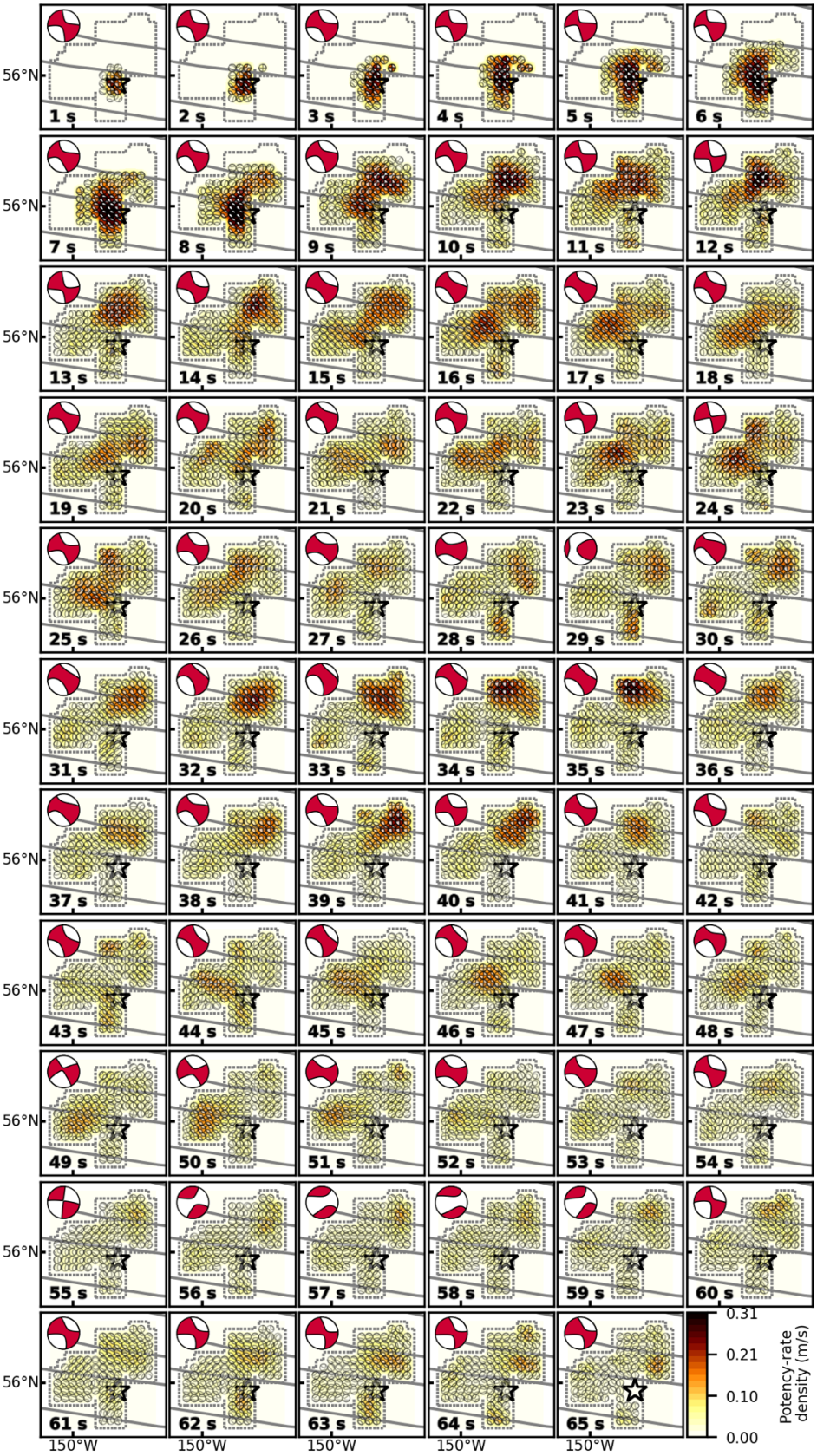
56°N
150°W
1 s
2 s
3 s
4 s
5 s
6 s
7 s
8 s
9 s
10 s
11 s
12 s
13 s
14 s
15 s
16 s
17 s
18 s
19 s
20 s
21 s
22 s
23 s
24 s
25 s
26 s
27 s
28 s
29 s
30 s
31 s
32 s
33 s
34 s
35 s
36 s
37 s
38 s
39 s
40 s
41 s
42 s
43 s
44 s
45 s
46 s
47 s
48 s
49 s
50 s
51 s
52 s
53 s
54 s
55 s
56 s
57 s
58 s
59 s
60 s
61 s
62 s
63 s
64 s
65 s
0.31
0.21
0.10
0.00
Potency-rate density (m/s)

Figure S12. Snapshots of the potency-rate density tensors every 1 s for the 2018 Gulf of Alaska earthquake. The dotted line shows the border of the assumed model plane. The star and solid lines indicate the epicenter (AEC) and the fracture zones (Matthews et al, 2011; Wessel et al., 2015), respectively. The large beachball in each panel indicates the corresponding total moment tensor at each time. This figure was made with matplotlib (v3.1.1; Hunter, 2007) and ObsPy (v1.1.0; Beyreuther et al., 2010).

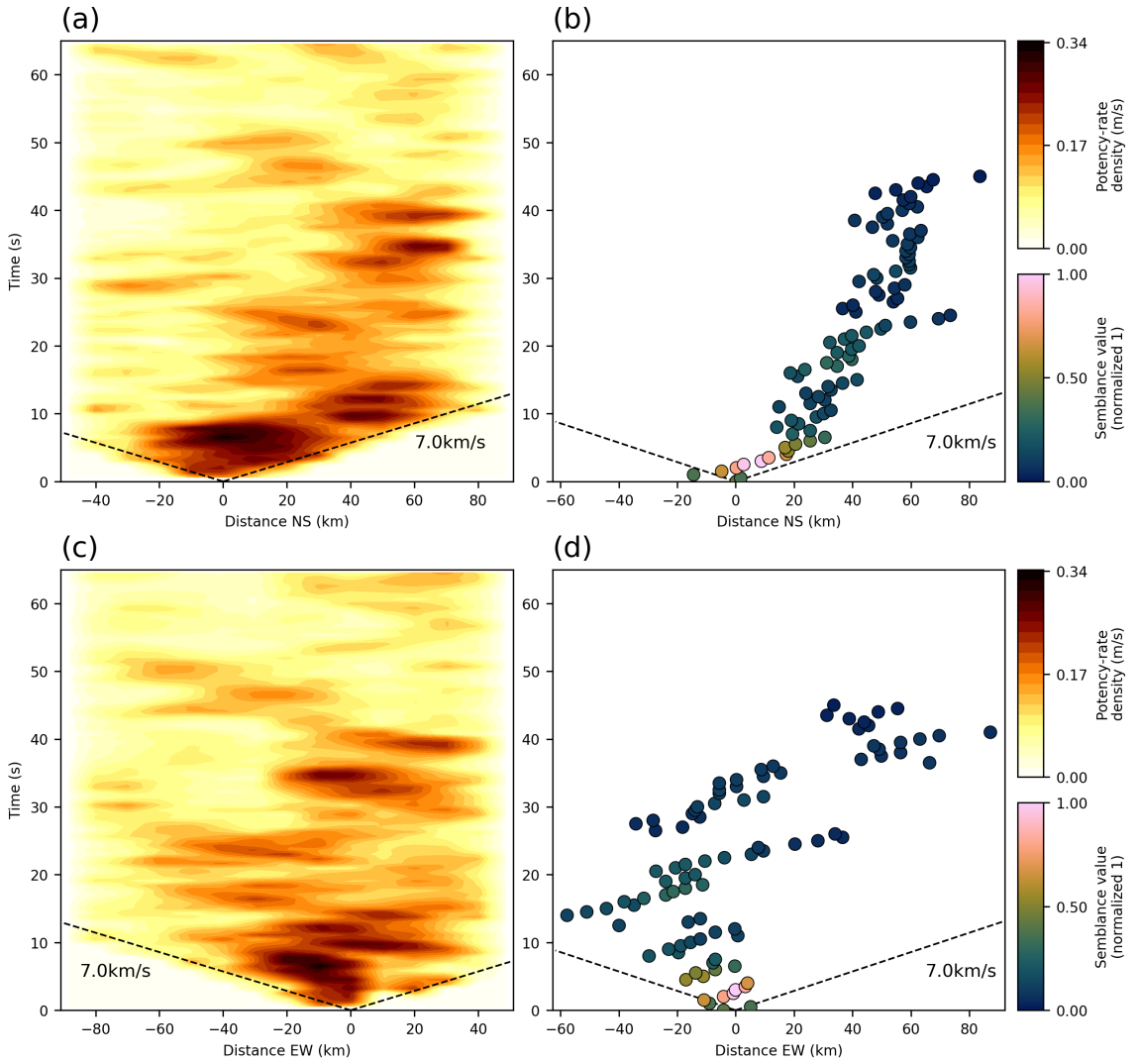

Figure S13. Comparison between the potency-rate density obtained by this study and the high-frequency (0.5-2.0 Hz) emissions obtained by Krabbenhoeft et al. (2018), projected along (a,b) north-south and (c,d) east-west directions from the epicenter. Positive distance directs toward (a,b) north and (c,d) east. Both the potency-rate density and semblance peaks distributions show general agreement in rupture pattern, especially during 0 to 10 s from the origin time. We note that a direct comparison or superimposing is not made here because our study and Krabbenhoeft et al. (2018) adopted the different reference-rupture points (epicenters). The dashed line represents the reference rupture speed. This figure was made with matplotlib (v3.1.1; Hunter, 2007).

Table S1. Factors of the smoothness constraint of each potency component for the numerical tests. The number $\boldsymbol{q}$ represents $\boldsymbol{M1}$ to $\boldsymbol{M5}$ components defined by Kikuchi and Kanamori (1991). $\left|\boldsymbol{m_q}\right|$ is the absolute value of the total potency derived from the input total moment tensor (Fig. S1b). The scaling factor $\boldsymbol{k}$ was set so that $\boldsymbol{min}(\boldsymbol{k}\left|\boldsymbol{m_q}\right|) = \boldsymbol{1}$.

q	1	2	3	4	5
$\lvert m_q \rvert$	1.0005	0.0000	0.0000	0.0000	0.0000
$k \lvert m_q \rvert$	10.0000	1.0000	1.0000	1.0000	1.0000

Table S2. CRUST1.0 structural velocity model (Laske et. al., 2013).

V_P (km/s)	V_S (km/s)	Density (10^3 kg/m^3)	Thickness (km)
1.50	0.00	1.02	4.30
1.85	0.41	1.87	0.39
5.00	2.70	2.55	0.66
6.50	3.70	2.85	1.47
7.10	4.05	3.05	4.53
8.08	4.49	3.33	0.00

Table S3. Factors of the smoothness constraint of each potency component for the analysis of the 2018 Gulf of Alaska earthquake. $\left|\boldsymbol{m_q}\right|$ is the absolute value of the total potency of each potency component derived from the GCMT solution (Fig. 1). The scaling factor $\boldsymbol{k}$ was set so that $\boldsymbol{min}(\boldsymbol{k}\left|\boldsymbol{m_q}\right|) = \boldsymbol{1}$.

q	1	2	3	4	5
$\lvert m_q \rvert$	0.7900	0.2500	0.3600	0.1900	0.2400
$k \lvert m_q \rvert$	4.1579	1.3158	1.8947	1.0000	1.2632

References

Beyreuther, M., Barsch, R., Krischer, L., Megies, T., Behr, Y., & Wassermann, J. (2010). ObsPy: A Python toolbox for seismology. *Seismological Research Letters*, 81(3), 530-533. https://doi.org/10.1785/gssrl.81.3.530

Bird, P. (2003). An updated digital model of plate boundaries. *Geochemistry, Geophysics, Geosystems*, *4*(3). https://doi.org/10.1029/2001GC000252

Dreger, D. S. (1994). Empirical Green's function study of the January 17, 1994 Northridge, California earthquake. *Geophysical research letters*, *21*(24), 2633-2636. https://doi.org/10.1029/94GL02661

Dziewonski, A. M., Chou, T. A., & Woodhouse, J. H. (1981). Determination of earthquake source parameters from waveform data for studies of global and regional seismicity. *Journal of Geophysical Research: Solid Earth*, *86*(B4), 2825-2852. https://doi.org/10.1029/JB086iB04p02825

Ekström, G., Nettles, M., & Dziewoński, A. M. (2012). The global CMT project 2004–2010: Centroid-moment tensors for 13,017 earthquakes. *Physics of the Earth and Planetary Interiors*, *200*, 1-9. https://doi.org/10.1016/j.pepi.2012.04.002

Fan, W., & Shearer, P. M. (2018). Coherent seismic arrivals in the P wave coda of the 2012 MW 7.2 Sumatra earthquake: Water reverberations or an early aftershock?. *Journal of Geophysical Research: Solid Earth*, *123*(4), 3147-3159. https://doi.org/10.1002/2018JB015573

Hartzell, S. H. (1978). Earthquake aftershocks as Green's functions. *Geophysical Research Letters*, *5*(1), 1-4. https://doi.org/10.1029/GL005i001p00001

Hunter, J. D. (2007). Matplotlib: A 2D graphics environment. *Computing In Science & Engineering*, *9*(03), 90-95. https://doi.ieeecomputersociety.org/10.1109/MCSE.2007.55

Kikuchi, M., & Kanamori, H. (1991). Inversion of complex body waves—III. *Bulletin of the Seismological Society of America*, *81*(6), 2335-2350.

Krabbenhoeft, A., von Huene, R., Miller, J. J., Lange, D., & Vera, F. (2018). Strike-slip 23 January 2018 MW 7.9 Gulf of Alaska rare intraplate earthquake: Complex rupture of a fracture zone system. *Scientific reports*, *8*(1), 1-9. https://doi.org/10.1038/s41598-018-32071-4

Laske, G., Masters, G., Ma, Z., & Pasyanos, M. (2013, April). Update on CRUST1. 0—A 1-degree global model of Earth's crust. In *Geophys. Res. Abstr* (Vol. 15, p. 2658).

Lawson, C. L., & Hanson, R. J. (1974). *Solving least squares problems,* Prentice-Hall, Englewood Cliffs., New Jersey.

Matthews, K. J., Müller, R. D., Wessel, P., & Whittaker, J. M. (2011). The tectonic fabric of the ocean basins. *Journal of Geophysical Research: Solid Earth*, *116*(B12). https://doi.org/10.1029/2011JB008413

Wessel, P., Matthews, K. J., Müller, R. D., Mazzoni, A., Whittaker, J. M., Myhill, R., & Chandler, M. T. (2015). Semiautomatic fracture zone tracking. *Geochemistry, Geophysics, Geosystems*, *16*(7), 2462-2472. https://doi.org/10.1002/2015GC005853

Wiens, D. A. (1987). Effects of near source bathymetry on teleseismic P waveforms. *Geophysical Research Letters*, *14*(7), 761-764. https://doi.org/10.1029/GL014i007p00761

Wiens, D. A. (1989). Bathymetric effects on body waveforms from shallow subduction zone earthquakes and application to seismic processes in the Kurile trench. *Journal of Geophysical Research: Solid Earth*, *94*(B3), 2955-2972. https://doi.org/10.1029/JB094iB03p02955

Yue, H., Castellanos, J. C., Yu, C., Meng, L., & Zhan, Z. (2017). Localized water reverberation phases and its impact on backprojection images. *Geophysical Research Letters*, *44*(19), 9573-9580. https://doi.org/10.1002/2017GL073254